iScience

CellPress
OPEN ACCESS

Article

Neural signaling modulates metabolism of gastric cancer

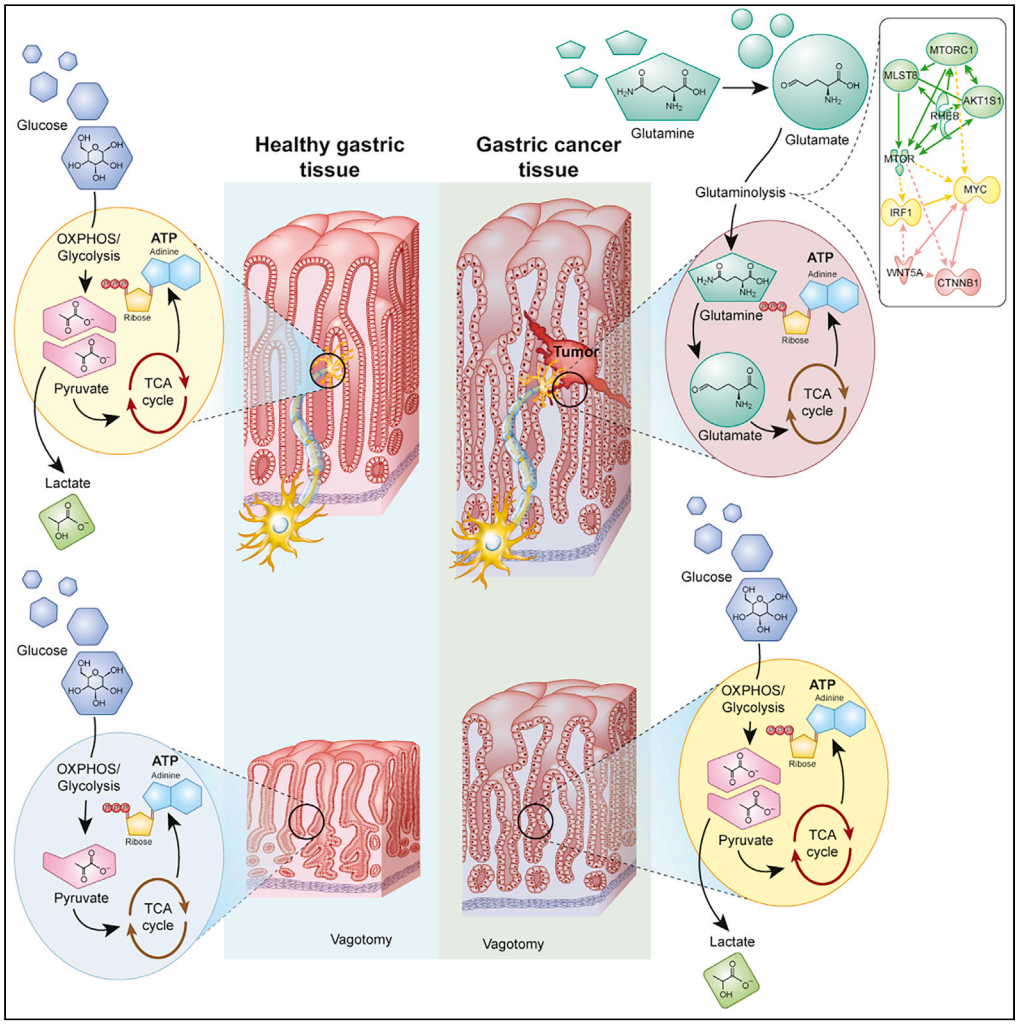

Hanne-Line Rabben, Gøran Troseth Andersen, Magnus Kringstad Olsen, ..., Jon Erik Grønbech, Duan Chen, Chun-Mei Zhao

chun-mei.zhao@ntnu.no

HIGHLIGHTS

Metabolic reprogramming in gastric cancer cells and tumor microenvironment

SNAP25, mTOR, PDP1/ α-KGDH, and glutaminolysis as potential drug targets

Combination of botulinum toxin type A, RAD001, and CPI-613 as a potential treatment

Rabben et al., iScience 24, 102091
February 19, 2021
https://doi.org/10.1016/j.isci.2021.102091

iScience

CellPress
OPEN ACCESS

Article

Neural signaling modulates metabolism of gastric cancer

Hanne-Line Rabben,[1,2,6] Gøran Troseth Andersen,[1,6] Magnus Kringstad Olsen,[1] Anders Øverby,[1] Aleksandr Ianevski,[1] Denis Kainov,[1] Timothy Cragin Wang,[1,3] Steinar Lundgren,[1,4] Jon Erik Grønbech,[1,5] Duan Chen,[1] and Chun-Mei Zhao[1,2,7,*]

SUMMARY

Tumors comprise cancer cells and the associated stromal and immune/inflammatory cells, i.e., tumor microenvironment (TME). Here, we identify a metabolic signature of human and mouse model of gastric cancer and show that vagotomy in the mouse model reverses the metabolic reprogramming, reflected by metabolic switch from glutaminolysis to OXPHOS/glycolysis and normalization of the energy metabolism in cancer cells and TME. We next identify and validate SNAP25, mTOR, PDP1/α-KGDH, and glutaminolysis as drug targets and accordingly propose a therapeutic strategy to target the nerve-cancer metabolism. We demonstrate the efficacy of nerve-cancer metabolism therapy by intratumoral injection of BoNT-A (SNAP25 inhibitor) with systemic administration of RAD001 and CPI-613 but not cytotoxic drugs on overall survival in mice and show the feasibility in patients. These findings point to the importance of neural signaling in modulating the tumor metabolism and provide a rational basis for clinical translation of the potential strategy for gastric cancer.

INTRODUCTION

Cancer is considered a genetic disease with tumor characteristics and metabolic reprogramming (Hanahan and Weinberg, 2011; Wishart, 2015; Whiteside, 2008). The tumor mass consists of primary tumor (i.e. cancer cells) and the associated stromal cells and immune/inflammatory cells, i.e. tumor microenvironment (TME) that usually is different from normal stroma. As cancer cells continue proliferation, the tumor increases in size with an associated remodeling of the TME that determines whether the primary tumor is eradicated, metastasizes, or establishes dormant micrometastases (Loponte et al., 2019; Yoshida, 2015; Vander Heiden and Deberardinis, 2017). The cancer metabolic reprogramming is reflected by alterations in the metabolic profiles of both cancer cells as well as TME. Cancer cells can activate glycolysis in the presence of adequate oxygen levels (aerobic glycolysis or the so-called Warburg effect) within TME, whereas cells of normally differentiated tissues obtain energy through the oxygen-dependent pathway of oxidative phosphorylation (OXPHOS) as well as through the oxygen-independent pathway of glycolysis (Liberti and Locasale, 2016). Emerging evidence suggests that the cancer metabolic reprogramming exhibits the following hallmarks: (1) deregulated uptake of glucose and amino acids, (2) use of opportunistic modes of nutrient acquisition, (3) use of glycolysis/tricarboxylic acid (TCA) cycle intermediates for biosynthesis and nicotinamide adenine dinucleotide phosphate (NADPH) production, (4) increased demand for nitrogen, (5) alterations in metabolite-driven gene regulation, and (6) metabolic interactions between cancer cells and the TME (Pavlova and Thompson, 2016). However, development of treatment targeting the cancer metabolic reprogramming has not yet been successful due to the large differences between tumor types and TME, thus this area is ripe for the strategic development of future targeted treatments for individual cancer types (Schulze and Harris, 2012; Coller, 2014; Liberti and Locasale, 2016; Wishart, 2015; Seyfried et al., 2014).

Gastric cancer (GC) is the fifth most common malignant disease worldwide with the third highest incidence and mortality rate among all cancers (Rawla and Barsouk, 2019). The 5-year overall survival rate for gastric cancer is 10%–30% except for Japan (50%–70%) (Parkin et al., 2005; Matsuda and Saika, 2013). Previously, we and others have demonstrated that vagotomy suppressed gastric tumorigenesis, suggesting a "nerve-cancer cell crosstalk" (Zhao et al., 2014; Hayakawa et al., 2017; Jobling et al., 2015; Wang et al., 2018). In the present study, we used the approaches of *in vitro*, *in vivo*, *in silico*, clinical evaluation, and pilot clinical trial,

[1]Department of Clinical and Molecular Medicine, Norwegian University of Science and Technology (NTNU), 7491 Trondheim, Norway

[2]The Central Norway Regional Health Authority, Norway

[3]Division of Digestive and Liver Diseases, Columbia University College of Physicians and Surgeons, New York, NY 10032-3802, USA

[4]Cancer Clinic, St. Olavs Hospital, Trondheim University Hospital, 7006 Trondheim, Norway

[5]Surgical Clinic, St. Olavs Hospital, Trondheim University Hospital, 7006 Trondheim, Norway

[6]These authors contributed equally

[7]Lead contact

*Correspondence: chun-mei.zhao@ntnu.no

https://doi.org/10.1016/j.isci.2021.102091

and employed the omics technology including comparative transcriptomics (human versus mouse), t-SNE, multi-omics (transcriptomics versus metabolomics), drug-target interaction prediction, and computational drug repositioning (Figure S1). We showed that the animal model we used mimicked GC patients in terms of tumor characteristics and metabolic reprogramming. We found that GC exhibited a metabolic reprogramming, i.e., the use of glutaminolysis for biosynthesis, that differed from other cancer types (Hanahan and Weinberg, 2011; Schulze and Harris, 2012) and that vagotomy reversed the metabolic reprogramming from glutaminolysis to OXPHOS/glycolysis in cancer cells as well as TME of the GC mice. We also identified the metabolic signature and validated the drug-target signaling interactions targeting nerve-cancer metabolism in human cancer cell lines and GC mice and developed a therapeutic strategy using a combination of denervation and cytotoxic free chemotherapy. This treatment appeared effective, particularly with regard to overall survival rate in aged GC mice, and showed potential in a pilot clinical trial in aged GC patients, suggesting a possible "metabolism-based" approach for GC (Figure S1. Study design, Related to Figure 1).

RESULTS

Human and mouse GC display similar metabolic reprogramming profile

Many studies on cancer metabolic reprogramming have been performed primarily in cancer cell lines to link "oncometabolites" to specific mutations of oncogenes. However, there has been a paucity of mechanistic studies in animal models of cancer investigating metabolic reprogramming, particularly any studies that have been closely linked with human studies or clinical trials (Deberardinis and Chandel, 2016). In the present study, we performed comparative transcriptomics using surgical biopsies of patients diagnosed with gastric adenocarcinoma and stomach samples from GC mice, i.e., the transgenic INS-GAS mice, which is a well-known model of spontaneous GC (Wang et al., 1996; Zhao et al., 2014; Fox and Wang, 2007). Human GC samples comprised of intestinal, diffuse, and mixed type adenocarcinoma, whereas mouse GC were predominantly of intestinal type. We compared transcriptomics profiles of the human GC tumor versus benign tissue in the same stomach and the mouse GC tumor versus normal tissue of wild-type (WT) mice. We found that the expression profile of signaling pathways was similar between human and mouse GC (Figures 1A, 1B, and 1D; Data S1. Canonical pathways in gastric cancer, Related to Figure 1). It should be noticed that the upregulated signaling pathways in both human and mouse GC included WNT/β-catenin; mTOR, PI3K/Akt, neuroinflammation, ERK/MAPK, HIPPO, and the CCK/gastrin-mediated pathway (which is specific for the stomach), and the downregulated signaling pathways included AMPK signaling, which is associated with OXPHOS, glycolysis, and fatty acid β-oxidation (Data S1). The expression profile of signaling pathways was confirmed by real-time PCR in which 89 genes related to WNT signaling pathway were measured (Table S1. Gene detected by real-time PCR and RNAseq, Related to Figure 1).

We then constructed a "GC metabolic gene expression profile" consisting of 140 genes that are involved in OXPHOS (37 genes), fatty acid β-oxidation (8 genes), carbohydrate metabolism (62 genes), and energy metabolism including the TCA cycle and glutaminolysis (34 genes). The GC metabolic gene expression profile was characterized by dysregulations of glutaminolysis and associated transporters of amino acids, the TCA cycle, carbohydrate metabolism, and fatty acid β-oxidation and displayed a positive correlation between human and mouse GC (Figures 2A, 2B, and 2D; Data S2. Metabolic genes in gastric cancer, Related to Figures 2 and 3). These results suggested that the mouse model of GC used in the present study would be useful for studying the molecular mechanisms of human GC metabolic reprogramming. Upstream regulator analysis of mouse RNA sequencing data from neoplastic lesions versus normal/healthy tissue revealed 144 regulators with increased activation whereof 8 regulators within the WNT/β-catenin signaling pathway—Tgf beta, WNT1, CD44, JUN, TGFB1, TGFBR1, TGFB2, and CTNNB1 (z-scores>2, $p < 0.05$)—were activated upstream of the mTOR pathway intermediates EIF3C, MRAS, PDPK1, RHOB, PPP2CA, PRKCG, and RHOA (Figure 2F; Table S2. Upstream regulators in mouse GC, Related to Figure 2F).

A single-cell atlas of gastric antral premalignant and early malignant mucosa has been recently constructed using single-cell mRNA sequencing data and visualized with t-distributed stochastic neighbor embedding (t-SNE) algorithm (Zhang et al., 2019). We performed t-SNE utilizing the gene expression data that are deposited at GEO (accession number GSE134520) (Zhang et al., 2019) and found that TCA cycle and glutaminolysis-dependent gene expression profile, particularly MDH1, MDH2, GLUL, IDH3B, DLD, SDHB, SLC17A5, SLC12A8, and OGDH, overlaid on the single-cell atlas of both cancer cells and TME (such as other proliferative cells, neck-like cells, pit mucous cells, enteroendocrine cells, T cells, and fibroblasts) (Figures 3A and 3B).

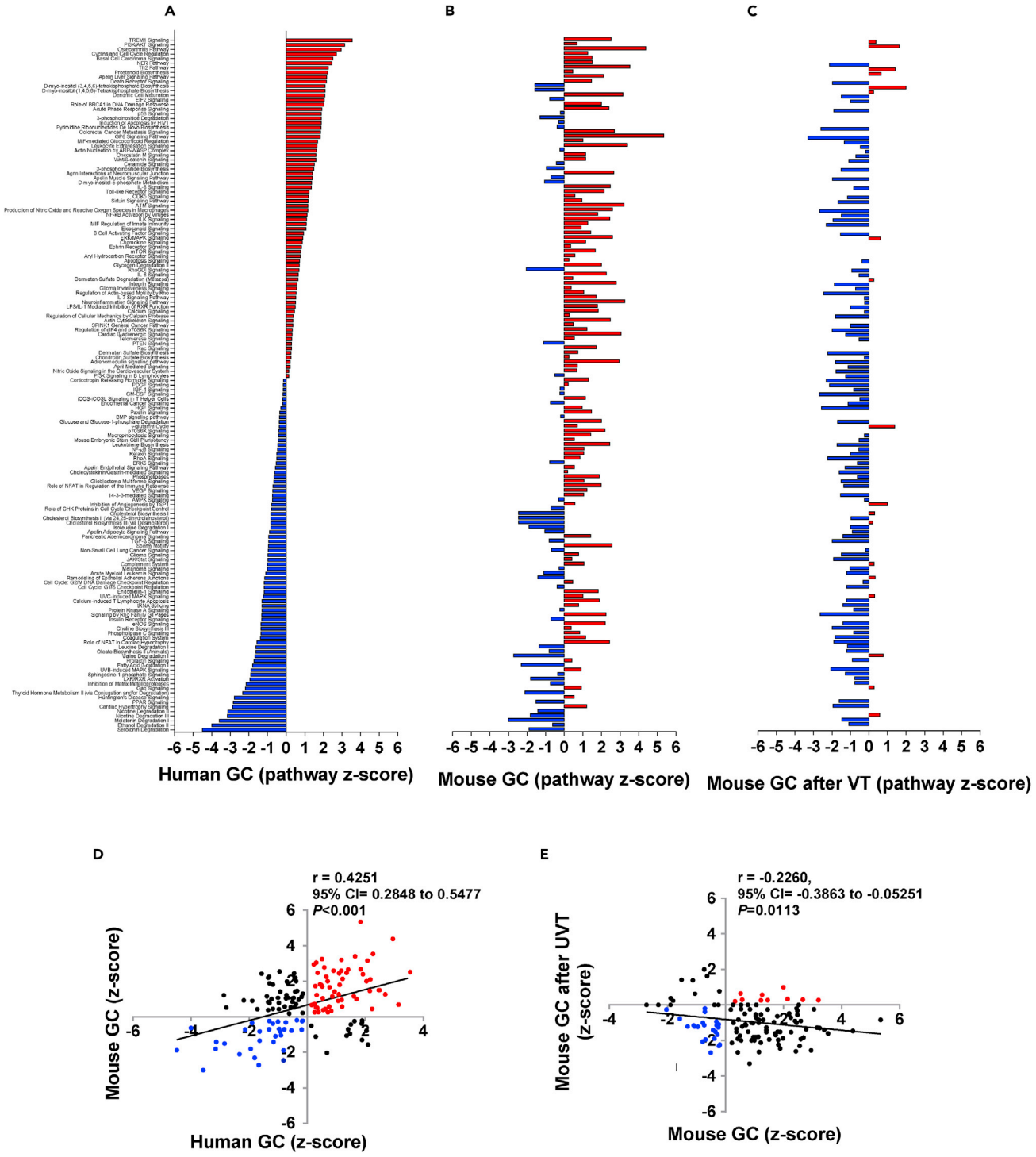

Figure 1. Signaling pathways in gastric cancer (GC)

Waterfall diagrams showing signaling pathways that were differentially activated (marked in red) and inhibited (blue) in human gastric cancer (GC) versus normal adjacent tissue (A) and mouse GC versus WT (B) or after vagotomy (C). Note: names of signaling pathways are listed in the same order in A–C. For detailed information, see Data S1.

Correlation between human and mouse GC (D) and mouse GC after vagotomy (E) in terms of Z-score. Z-scores were generated in IPA using datasets with differently expressed genes ($p < 0.05$). Pearson's test was used for correlation, and a linear regression line was drawn using GraphPad Prism v6. UVT in E: unilateral vagotomy (which results in innervated and denervated sides within the same stomach).

For study groups, see Table S12 (Study groups, Related to Figures 7K and 8G–8L).

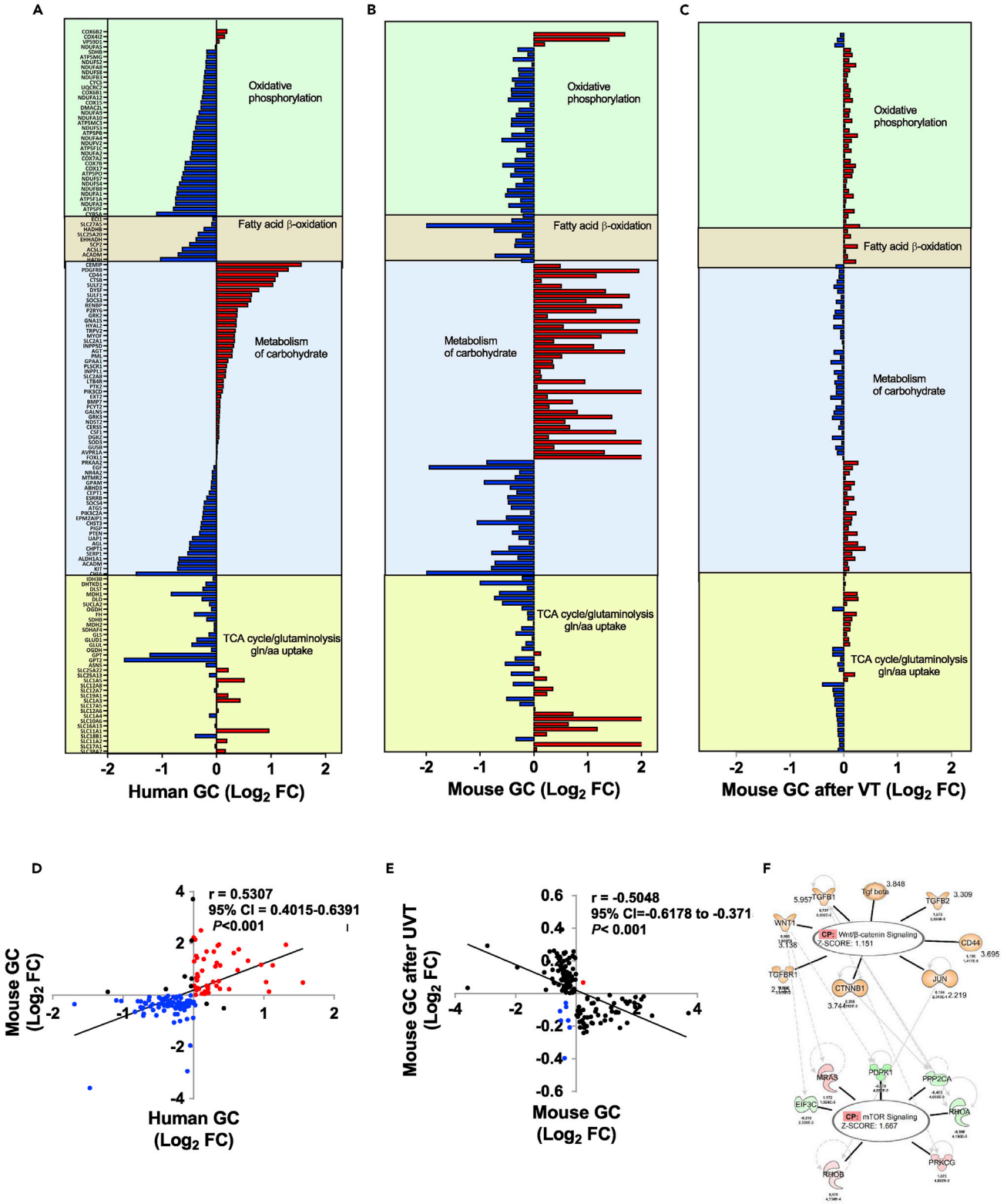

Figure 2. Metabolic gene expression profiles in gastric cancer (GC)

Waterfall diagrams showing metabolic gene expression profiles of human gastric cancer (GC)(A), mouse GC (B), and mouse GC (6 months after vagotomy (VT)(C). Note: names of genes are listed in the same order in A–C and differentially expressed genes in upregulation (marked in red) and downregulation

Figure 2. *Continued*
(blue). For detailed information, see Data S2. Pearson's test was used for correlation, and a linear regression line was drawn using GraphPad Prism v6. UVT in E: unilateral vagotomy (which results in innervated and denervated sides within the same stomach). Upstream regulator analysis of mouse GC transcriptomics performed in IPA revealed regulators of the WNT/β-catenin signaling pathway being upstream of mTOR signaling (F).
Orange: predicted activated; Blue: predicted inhibition; Green: downregulated; Red: upregulated; Gray: did not pass p value cut-off. Annotated with $\log_2$ fold change, p value, and z-scores, see Table S2.

Vagotomy reverses the metabolic reprogramming of GC

Vagal innervation is known to regulate epithelial cell proliferation in the stomach and has recently been implicated in GC development and progression (Hayakawa et al., 2017; Wang et al., 2018; Zhao et al., 2014; Zahalka and Frenette, 2020). Vagal denervation can be achieved surgically, pharmacologically, or genetically. The surgery includes bilateral truncal vagotomy or unilateral truncal vagotomy (UVT). UVT takes advantage of the fact that each (anterior or posterior) vagal trunk innervates only one-half of the stomach, and consequently, UVT does not impair the overall function of the stomach. In a previous study, we showed that vagotomy during the pre-neoplastic stage of tumorigenesis diminished tumor incidence and size, and attenuated tumor cell proliferation specifically in the denervated portion of the stomach, suggesting that the vagus nerve promotes gastric cancer growth. Consistent with this idea, pharmacologic denervation via local injection of botulinum toxin A (BoNT-A) into the gastric wall similarly impaired pre-neoplastic growth. Furthermore, vagotomy or BoNT-A treatment at later stages of tumorigenesis suppressed GC progression and augmented the antitumor effect of cytotoxic chemotherapy in tumor-bearing mice, resulting in prolonged survival (Zhao et al., 2014). In the present study, we further examined the effect of vagotomy on the metabolic reprogramming of GC. In a comparison between the innervated and denervated GC mouse stomachs after UVT, the expression profiles of signaling pathways as well as the metabolic genes were reversed after vagotomy activities and displayed negative correlations between the two sides of stomach after UVT (Figure 1B versus 1C; 2B versus 2C; 1E, 2E; Data S1 and S2).

We then performed metabolomics analysis of gastric tissues in GC and WT mice that underwent UVT. By comparison of GC between innervated tumors and denervated tumors, we identified 48 dysregulated metabolites representing a "metabolic signature" of GC, and furthermore we found that the levels of metabolites, regardless of the direction of change in individual metabolites, were reversed after vagotomy to the normal levels of WT mice (Figure 4A; Table S3. Metabolite signature, Related to Figure 4; Table S13. Metabolite involved with DNA/protein syntheses, Related to Figure 4). We suggest that the metabolic signature of GC reflects the changes in both cancer cells and TME rather than specific mutations of oncogenes (i.e. "oncometabolites"). Among the metabolites in the metabolic signature of GC, some metabolites such as prostaglandin E2, methionine, and glycine are known to be abundant in GC (Uefuji et al., 2000; Wang and Dubois, 2018; Sanderson et al., 2019; Hirayama et al., 2009). Of note, the effects of vagotomy on the metabolites were different between WT and GC mice, suggesting a different response of denervation on normal tissue compared with tumor tissue (Figure 4A; Table S3; Data S3. Metabolites measured by LC/MS and GC/MS by Metabolon, Related to Figures 4 and S2A–S2D). These results corresponded well to changes in the metabolic gene expression profile, suggesting that vagotomy reversed the metabolic reprogramming of GC at both transcript and metabolite levels.

We next focused on the effects of vagotomy on tumor energy metabolism encompassing the OXPHOS/glycolysis (including the Warburg effect), glutaminolysis, and the TCA cycle (Figures 4B–4N; Table S4. Energy metabolites, Related to Figures 4B–4N). Metabolic flexibility of the tumor involves anaplerotic steps in energy metabolism (Smith et al., 2018). In comparison with WT mice, GC mice displayed an increased glutaminolytic flux through the TCA cycle, which was reflected by higher levels of glycine, oxidized glutathione (GSSG), citrate, 5-oxoproline, cis-aconitate, L-glutamate, L-glutamine, and threonine (Figures 4B, 4C, 4E, 4F, 4I, 4J, 4K, and 4N) but not the glycolysis (represented by glucose, lactate, and fructose-6-phosphate) (Figures 4G, 4L, and 4M). After vagotomy, the glutaminolysis, but not glycolysis, intermediates were reduced in GC mice (Figure 4). Comparison of GC after vagotomy versus WT without vagotomy revealed no difference in the energy metabolism (Figures 4B–4N and S2A–S2D), suggesting that vagotomy in GC mice led to a normalization of the energy metabolism. However, WT mice responded to vagotomy differently compared with GC mice, namely having reduced glutaminolysis as well as glycolysis (Figures 4B–4N and S2A–S2D. Gastric cancer is glutamine-dependent, Related to Figure 4; Table S4).

To confirm that GC was dependent on glutamine and/or pyruvate, we measured endogenous L-glutamine and L-glutamate levels in human gastric adenocarcinoma cell line (AGS cells). We found stable levels of

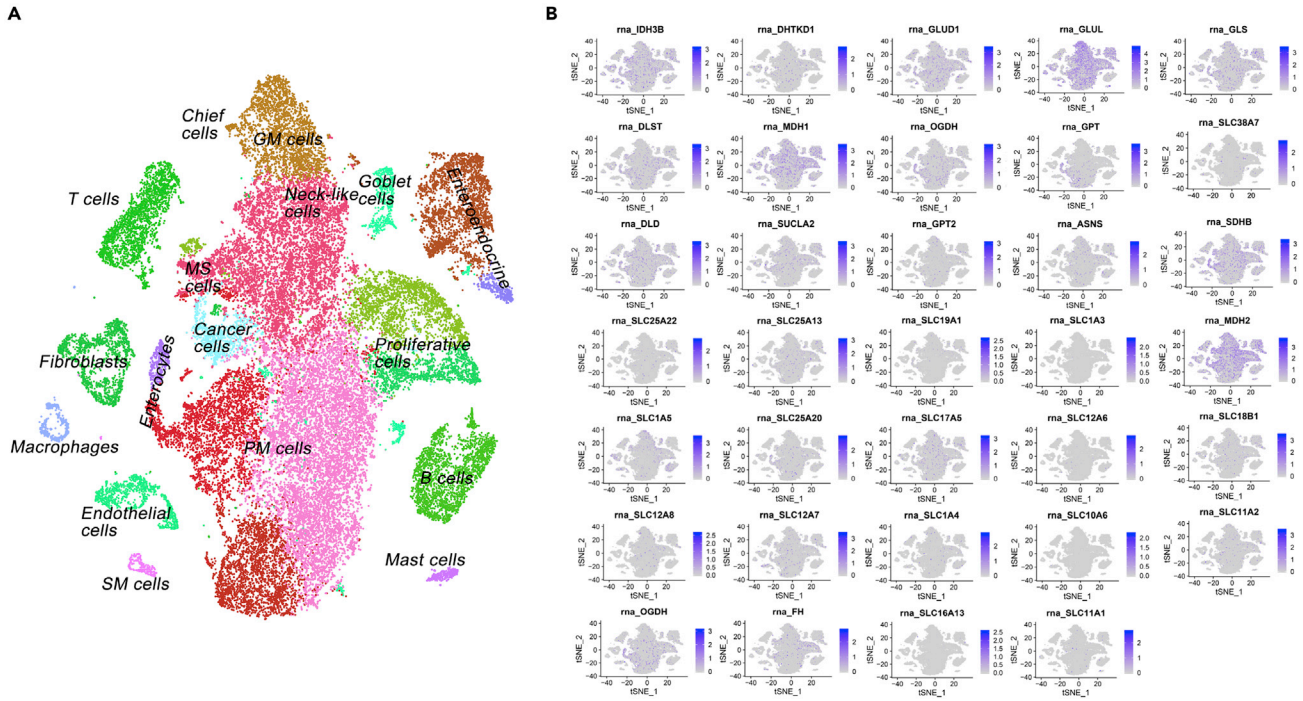

Figure 3. Glutamine-dependent gene expression profile of gastric cancer (GC) according to the single-cell atlas

tSNE plot of single-cell data released by the study of premalignant lesions and gastric cancer (Zhang et al., 2019) (A). The expression patterns of 34 TCA/glutaminolysis/gln uptake genes according to Figure 2 (B). Single-cell data were processed using Seurat v3 (https://doi.org/10.1016/j.cell.2019.05.031). Data was normalized for each of the 13 samples independently, followed by the functions FindIntegrationAnchors, IntegrateData, ScaleData, and RunPCA with default parameters. As in the original study, cells with number of expressed genes lower than 400 or larger than 7,000 were removed, and 20% or more of UMIs were mapped to mitochondrial or ribosomal genes. 50 PCs were utilized to visualize the single-cell atlas with a tSNE plot.

L-glutamine and L-glutamate during a culture period of 1–24 h (Figure S2E). We further performed *in vitro* experiments in AGS and MKN45 cells (both human gastric adenocarcinoma cell lines). The proliferation rates of both cells were time and concentration dependent on glutamine (Figures S2, S2F, and S2G). Moreover, the cell proliferation was reduced and eventually stopped 24–72 h after depletion of glutamine but not pyruvate (Figures S2, S2H, and S2I). These results confirmed that GC cells were glutamine dependent.

Vagotomy alters neuronal, metabolic, and WNT-mTOR signaling pathways in GC

To explore the signaling pathways by which vagotomy reverses metabolic reprogramming in GC mice, we performed integrative omics (multi-omics) of transcriptomics versus metabolomics and found the signaling pathways associated with metabolism, such as synaptogenesis signaling pathway, endocannabinoid neuronal synapse pathway, role of MAPK signaling, neuroinflammation signaling pathway, glutamate receptor signaling, glutathione biosynthesis, glutamate degradation II, and UDP-N-acetyl-D-glucosamine biosynthesis II (Figure 5A; Table S5. Signaling pathways involved in mouse gastric cancer, Related to Figure 5A). We also found that metabolite-related signaling pathways, such as synaptic long-term depression, triacylglycerol biosynthesis, and CDP-diacylglycerol biosynthesis I were attenuated after vagotomy, whereas antioxidant action of vitamin C and purine nucleotides *de novo* biosynthesis II were activated, suggesting compensatory responses after vagotomy (Figure 5B; Table S6. Signaling pathways involved in mouse gastric cancer after vagotomy, Related to Figure 5B). Furthermore, vagotomy in GC mice reversed or restored the signaling pathways of "WT" phenotype, including TCA cycle II (eukaryotic), protein kinase A signaling, calcium signaling, gap junction signaling, and phospholipases (Figure 5C; Table S7. Signaling pathways involved in mouse gastric cancer with and without vagotomy, Related to Figure 5C). The results were in line with the signaling pathways revealed by transcriptomics showing that WNT/β-catenin signaling and mTOR signaling were inhibited after vagotomy (Data S1) and in agreement with our previous study showing that vagotomy reduced the expression of WNT-regulated stem cell markers and decreased the expansion of leucine-rich repeat containing G-protein-coupled receptor 5-positive ($LGR5^{+}$) stem cells in the gastric mucosa (Zhao et al., 2014). Other reports showed that mTORC1/2 activity was associated

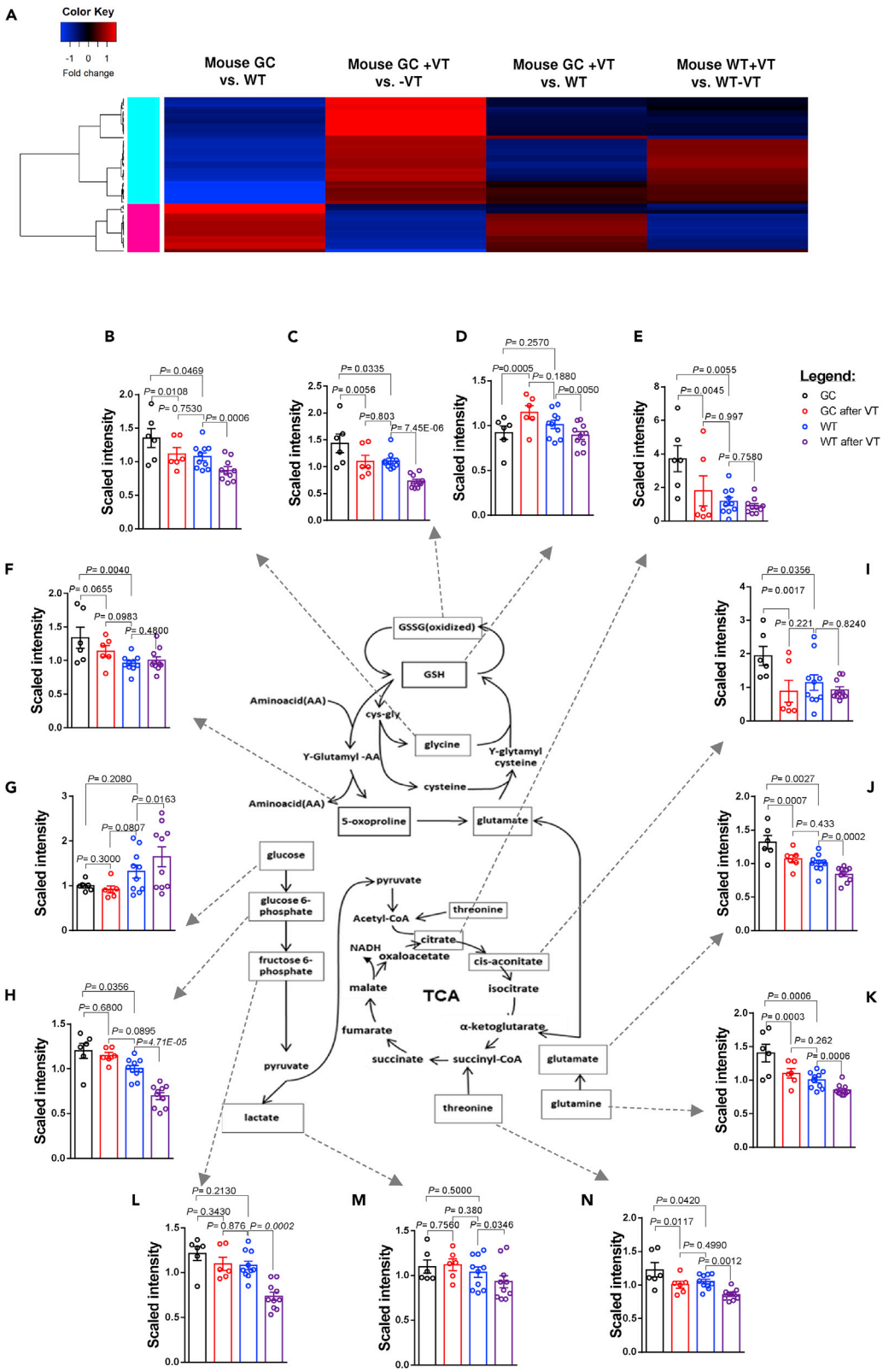
A
Color Key
-1 0 1
Fold change
Mouse GC vs. WT
Mouse GC +VT vs. -VT
Mouse GC +VT vs. WT
Mouse WT+VT vs. WT-VT
B
C
D
E
Legend:
GC
GC after VT
WT
WT after VT
Scaled intensity
F
G
H
I
J
K
L
M
N
GSSG(oxidized)
GSH
Aminoacid(AA)
cys-gly
glycine
Y-Glutamyl -AA
Y-glytamyl cysteine
cysteine
5-oxoproline
glutamate
glucose
glucose 6-phosphate
fructose 6-phosphate
pyruvate
Acetyl-CoA
threonine
citrate
NADH
oxaloacetate
cis-aconitate
malate
TCA
isocitrate
fumarate
α-ketoglutarate
succinate
succinyl-CoA
glutamine
lactate

Figure 4. Effects of vagotomy on metabolite levels in wild-type (WT) and gastric cancer (GC) mice

Heatmap showing metabolite fold changes of mouse gastric cancer (GC) versus wild-type (WT), mouse GC after unilateral vagotomy (VT), i.e. innervated versus denervated sides within the same stomach, mouse GC after VT versus WT mice, and mouse WT after VT, i.e. innervated versus denervated sides within the same stomach (A). Color key shows fold change in red (increase) or blue (decrease), generated using differently expressed metabolites ($p < 0.05$) in mouse GC versus WT (1) and mouse GC after VT (2) with the heatmap.2 function in RStudio version 3.5.2. For detailed information, see Table S3 and Data S3. Energy metabolism after VT (B–N): levels of metabolites in energy metabolism encompassing OXPHOS/glycolysis/Warburg effect, glutaminolysis, and TCA (B-N). Metabolites in mouse gastric cancer (GC) (marked in black), wild-type WT (blue), GC after VT (red), and WT after VT (purple). Glu: L-glutamate; Gln: L-glutamine; GSH: reduced glutathione; GSSG: oxidized glutathione; Gly: glycine; Thr: threonine; Oxo: 5-oxoproline; C-at: cis-aconitate; Glc: glucose; G6P: glucose-6-phosphate; F6P: fructose-6-phosphate.

Bars represent means of n = 6 (GC) or n = 10 (WT) relative scaled intensities with SEM and one-way ANOVA p values. For detailed information, see Table S4 and Figures S2A–S2D.

with glutamine-dependent anaplerosis (Liao et al., 2019; Duran et al., 2012). Taken together, the results suggested that glutaminolysis, neuronal signaling, WNT/β-catenin signaling, and mTOR signaling of GC were altered by vagotomy, and thus might represent potential therapeutic targets.

Drug-target interaction prediction shows SNAP25, mTOR, PDP1/α-KGDH, and glutaminolysis as drug targets

We next performed drug-target interaction prediction and computational drug repositioning of approved and investigational drugs/compounds (e.g. existing at the website of ClinicalTrials.gov) in GC mice and patients. We identified the network nodes (i.e. drug targets) at the levels of proteins, mRNAs, microRNA, and metabolites with special focus on the following four targets with potential drugs: SNAP25 with BoNT-A, mTOR with RAD001 (also known as Everolimus), PDP1/α-KGDH with CPI-613, and GLS with DON, 968, CB839, or BPTES in both GC mice and patients (Figures 6 and S3. Drug target prediction, Related to Figure 6). In our previous study, we have demonstrated that either local vagotomy or local injection of BoNT-A suppresses GC (Zhao et al., 2014). This was most likely because BoNT-A binds selectively to synaptosomal nerve-associated protein 25 (SNAP25), which is an integral protein required for docking and release of acetylcholine from vesicles situated in the vagal nerve endings (Naumann and Jankovic, 2004; Dressler et al., 2005). RAD001 is a rapamycin analog that specifically inhibits the mTORC1 complex by binding to FKBP12 (Faivre et al., 2006). The enzymes pyruvate dehydrogenase (PDH/PDP1) and α-ketoglutarate dehydrogenase (α-KGDH) control acetyl-CoA/pyruvate and glutamine/glutamate anaplerotic steps to the TCA cycle, respectively. The lipoate analog CPI-613 (6,8-Bis[(phenylmethyl)thio-octanoic acid) inhibits both enzymes (Dorsam and Fahrer, 2016; Lee et al., 2014; Pardee et al., 2014; Stuart et al., 2014; Zachar et al., 2011). Glutaminase inhibitors, such as CB-839, BPTES, DON, and 968, have been tested in a variety of cancers (Fung and Chan, 2017) but have limited efficacy and considerable adverse effects. It should also be noticed that the WNT signaling pathway did not appear as drug-target *per se*, as there are no drugs yet developed (Kahn, 2014). Thus, we tested neither the glutaminase inhibitors nor any inhibitors of the WNT signaling pathway in the present study. Next, we performed *in vitro* experiments to validate the efficacies of these potential metabolic-targeted therapies. Treatment of human GC cells with either RAD001 or CPI-613 reduced cell proliferation in dose-dependent manners (Figures 7A–7D). Combination of both inhibitors at IC_{50} doses for either 24 or 48 h resulted in synergistic inhibition (Figures 7E–7G). We found that BoNT-A alone was without any significant concentration-dependent inhibition on cell proliferation and did not enhance the inhibitory effects of neither 5-FU and/or oxaliplatin nor RAD001 and/or CPI-613 in any range of concentration responses (Figure S4. *In vitro* drug screening, Related to Figure 7), suggesting that the cytotoxic effect of BoNT-A on the cells does not take place *in vitro*. We also found that combination of RAD001 and CPI-613 had similar inhibitory effect with or without adding 5-FU and/or oxaliplatin (Figure S4).

Preclinical trial shows therapeutic effects of nerve-cancer metabolism therapy for GC

Previously, we demonstrated that gastric denervation by either vagotomy or local BoNT-A injection had similar anti-tumor effects (Zhao et al., 2014). Vagotomy can be performed at open surgery (laparotomy) or using minimally invasive surgery (laparoscopy), whereas pharmacological denervation by BoNT-A injection into the gastric wall can be achieved through gastroscopy, which is much less invasive in comparison with laparoscopic vagotomy.

Many GC patients are elderly who have poor tolerance to the current therapeutic options including subtotal or total gastrectomy with radical lymph node dissection, adjuvant chemoradiotherapy, or perioperative chemotherapy. Systemical use of cytotoxic drug treatment in elderly patients is usually associated with concerns regarding quality of life and overall survival (OS). Thus, the therapeutic strategy should be focused on

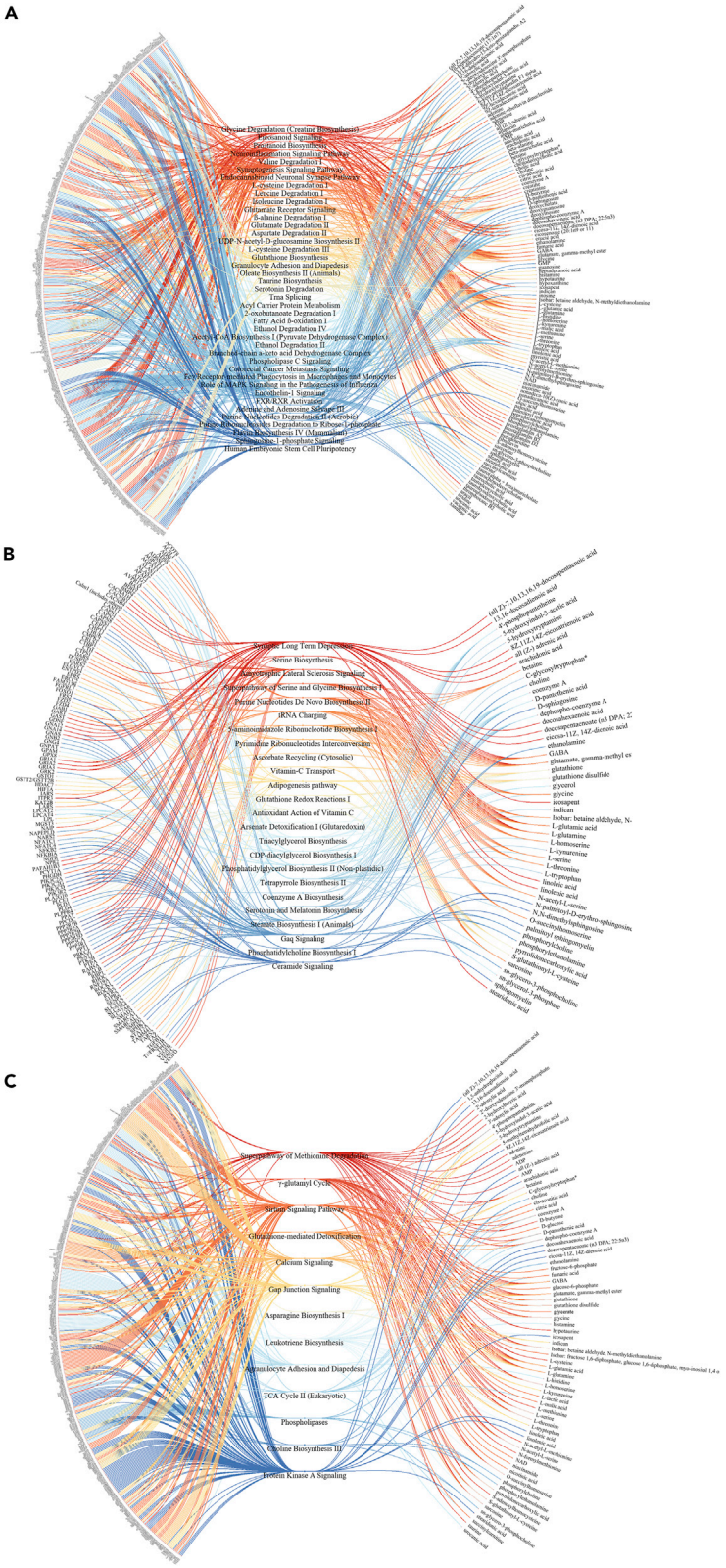
A
Glycine Degradation (Creatine Biosynthesis)
Phytanoyl-2-hydroxylase Signaling
Ecdysteroid Biosynthesis
Nitrogen Repletion Signaling Pathway
Valine Degradation I
Synaptogyrin Signaling Pathway
Endocannabinoid Neuronal Synapse Pathway
L-cysteine Degradation I
Leucine Degradation I
Isoleucine Degradation I
Glutamate Receptor Signaling
b-alanine Degradation I
Glutamate Degradation II
Aspartate Degradation II
UDP-N-acetyl-D-glucosamine Biosynthesis II
L-cysteine Degradation III
Glutathione Biosynthesis
Granulocyte Adhesion and Diapedesis
Oleate Biosynthesis II (Animals)
Taurine Biosynthesis
Serotonin Degradation
Trna Splicing
Acyl Carrier Protein Metabolism
2-oxobutanoate Degradation I
Fatty Acid b-oxidation I
Ethanol Degradation IV
Acetyl-CoA Biosynthesis I (Pyruvate Dehydrogenase Complex)
Ethanol Degradation II
Branched-chain a-keto acid Dehydrogenase Complex
Phospholipase C Signaling
Colorectal Cancer Metastasis Signaling
Fcγ Receptor-mediated Phagocytosis in Macrophages and Monocytes
Role of MAPK Signaling in the Pathogenesis of Influenza
Cholecystokinin/Gastrin-mediated Signaling
Leukotriene Signaling
LXR/RXR Activation
Adenine and Adenosine Salvage III
Purine Nucleotides Degradation II (Aerobic)
Purine Ribonucleosides Degradation to Ribose-1-phosphate
Platelet Activating Factor Signaling
Sphingosine-1-phosphate Signaling
Human Embryonic Stem Cell Pluripotency
B
Synaptic Long Term Depression
Serine Biosynthesis
Amyotrophic Lateral Sclerosis Signaling
Superpathway of Serine and Glycine Biosynthesis I
Purine Nucleotides De Novo Biosynthesis II
tRNA Charging
5-aminoimidazole Ribonucleotide Biosynthesis I
Pyrimidine Ribonucleotides Interconversion
Ascorbate Recycling (Cytosolic)
Vitamin-C Transport
Adipogenesis pathway
Glutathione Redox Reactions I
Antioxidant Action of Vitamin C
Arsenate Detoxification I (Glutaredoxin)
Triacylglycerol Biosynthesis
CDP-diacylglycerol Biosynthesis I
Phosphatidylglycerol Biosynthesis II (Non-plastidic)
Tetrapyrrole Biosynthesis II
Coenzyme A Biosynthesis
Serotonin and Melatonin Biosynthesis
Stearate Biosynthesis I (Animals)
Gap Signaling
Phosphatidylcholine Biosynthesis I
Ceramide Signaling
C
Superpathway of Methionine Degradation
γ-glutamyl Cycle
Sirtuin Signaling Pathway
Glutathione-mediated Detoxification
Calcium Signaling
Gap Junction Signaling
Asparagine Biosynthesis I
Leukotriene Biosynthesis
Agranulocyte Adhesion and Diapedesis
TCA Cycle II (Eukaryotic)
Phospholipases
Choline Biosynthesis III
Protein Kinase A Signaling

Figure 5. Multi-omics in gastric cancer (GC)

"Butterfly" diagrams showing signaling pathways (in center) that overlap with a significant Fisher's test ($p < 0.05$) between transcriptomics (left panel) and metabolomics datasets (right panel) in comparison between mouse gastric cancer (GC) versus wild-type (A), GC with versus without innervation (after VT) (B), and both GC versus WT and GC after VT (C). Diagram plots were created with JavaScript library D3.js v4. For detailed information, see Tables S5–S7.

the clinical endpoints, including OS and quality of life and, to lesser extent, tumor size. Thus, we performed different treatments of GC mice at 9–15 months of age and followed-up as long as the mice lived (maximal 14 months after starting treatment). Treatments included 5-FU plus oxaliplatin (named FUOX) and combinations of gastric injection of BoNT-A, RAD001, and CPI-613 (named BRC) with or without FUOX for 2 months (Figure 7H), and mice were followed-up by measuring OS, median survival (MS) time, body weight changes, and tumor size. We found that OS and MS were 33% and 148 days, respectively, in GC mice without any treatment (age-matched controls, AMC), 40% and 40 days in GC mice that received either FUOX or BRC + FUOX, but 90% and 249 days in GC mice that received BRC in comparisons with AMC (Figure 7I). Of note, the survival rates in mice with cytotoxic drugs *per se* (i.e. FUOX) or in combination with BRC were worse than mice without any treatment. Quality of life in mice can be measured by body weight change. FUOX induced body weight loss to the human endpoint (i.e. 25% of initial weight or less than 25% but with poor physical appearance) during the treatment period. BRC induced about 10% weight loss during the treatment and attenuated the weight loss by FUOX (Figure 7J). Within the treatment period of 2 months, 5-FU and oxaliplatin given either alone or as FUOX did not reduce the tumor size, RAD001 and CPI-613 given either alone or in combination also did not reduce the tumor size, whereas BoNT-A alone reduced the tumor size and had synergic effects when given together with FUOX or as BRC + FUOX (Figure 7K). There was no difference in tumor size between FUOX and BRC + FUOX (Figure 7K). Thus, these results suggested that BoNT-A *per se* had no cytotoxic effect *in vivo* and that BRC (BoNT-A + RAD001+-CPI-613 without 5-FU and/or oxaliplatin) increased OS and MS, suggesting a potential cytotoxic chemo-free therapy for GC.

In order to verify the mechanism of action, we performed transcriptomic profiling with focus on the gene expression profile of glutaminolysis-WNT-mTOR-c-MYC signaling pathways and found that vagotomy and treatment with metabolic inhibitors with or without pharmacological denervation, i.e., RC or BRC, in GC mice for 2 months reversed the gene expression profile of glutaminolysis-WNT-mTOR-c-MYC signaling pathway, suggesting a possible mechanism of "nerve-cancer metabolism therapy" (Figures 8 and S5A–S5D. Nerve-cancer metabolism in gastric cancer, Related to Figure 8A), supporting that BRC is a nerve-cancer metabolism therapy for GC. We further analyzed the gene expression pattern of glutaminolysis-WNT-mTOR-c-MYC signaling pathway in GC mice based on the single-cell transcriptome atlas of (human) stomach (Zhang et al., 2019) and found that the upregulated gene expression was reversed after vagotomy, RC or BRC in both cancer cells and TME (e.g. T cells, B cells, macrophages, fibroblast, mast cells, and endothelial cells) (Figure 8B), suggesting that the nerve-cancer metabolism therapy acts on both cancer cells and TME in GC. Furthermore, computational network modeling revealed intensive connections across the genes within the cell type and with the genes involved in glutaminolysis (Figures 8C, 8D, and S6A–S6E. Single-cell atlas and glutamine pathways, Related to Figures 8C and 8D).

WNT-signaling induces activation of mTORC1 signaling through the inhibition of GSK3β (Shimobayashi and Hall, 2014) or through induction of MYC in a CTNNB1-dependent manner (Zhang et al., 2012; Grigoryan et al., 2013). We next performed an *in silico* experiment to predict the effects of inhibition of nodes/genes in WNT/β-catenin network on mTOR network and *vice versa*, which are based on both experimental data, the Ingenuity Knowledge Base, and peer-reviewed literature. We first constructed two functional cluster networks of WNT/β-catenin and mTOR signaling based on the gene expression profile of GC mice (Figure 8E), and the *in silico* testing by inhibition of β-catenin (CTNNB1), c-MYC (MYC), or WNT7B either alone or in combination with other genes/nodes within the cluster showed that the inhibition of WNT/β-catenin network led to inhibition of the mTOR cluster, whereas inhibition of the mTOR kinase or mTORC1 complex either alone or in combination with other genes/nodes within the cluster was without inhibition on the WNT/β-catenin cluster (Figures 8F and S7A. *In silico* modeling, Related to Figure 8), probably suggesting a downstream signal flow in WNT-mTOR signaling pathways. Of note, inhibition of either Frizzled, GSK3β, or DVL nodes alone was without effect on mTOR cluster. As expected, functional cluster networks of both WNT/β-catenin and mTOR as predicted through *in silico* testing were inhibited 2 months after RC in GC mice (Figure S7B. *In silico* modeling, Related to Figure 8).

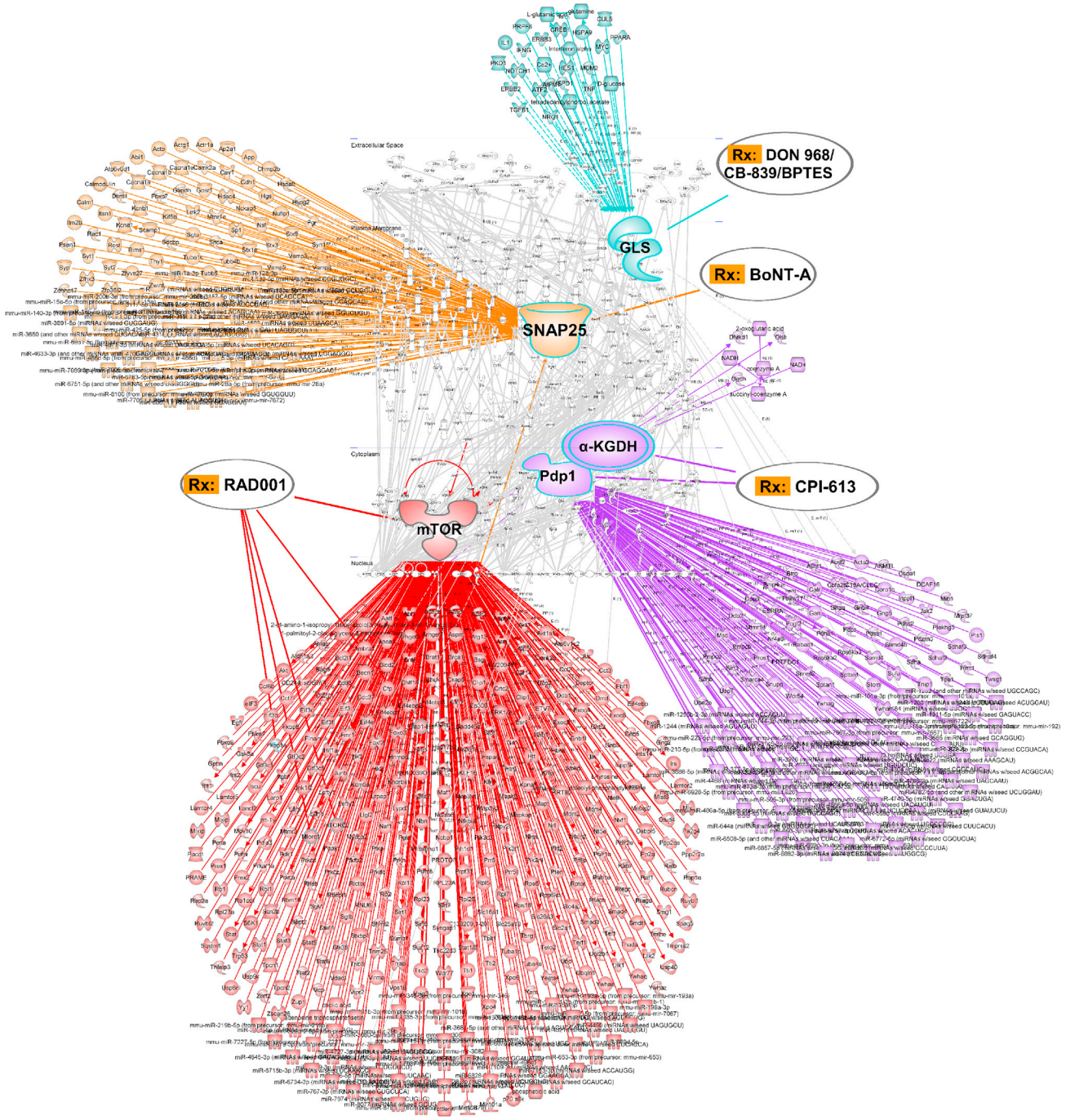

Figure 6. Drug target prediction and repurposing

"Waterdrop" diagrams showing drug-target. Interaction prediction and computational drug repositioning from transcriptomics data in mouse GC created in Ingenuity Pathway Analysis (IPA). Note: nodes of RAD001-targeted mTOR (marked in red), CPI-613-targeted PDP1 and/or α-KGDH (purple), BoNT-A-targeted SNAP25 (yellow), and DON/968/CB-839/BPTES-targeted GLS (light blue). Lines represent biological relationships between molecules that include proteins, genes, mRNAs, microRNAs, and metabolites, generated from differentially expressed drug target genes (only drug targets differentially expressed between mouse GC versus WT at $p < 0.05$, $q < 0.05$ are shown, light gray). Molecule nodes are fetched from RNA sequencing data in mouse GC versus WT, edges are generated based on causal information in the Ingenuity Knowledge Base. The overlay-tool in IPA is used to predict drugs for indicated nodes.

See also Figure S3.

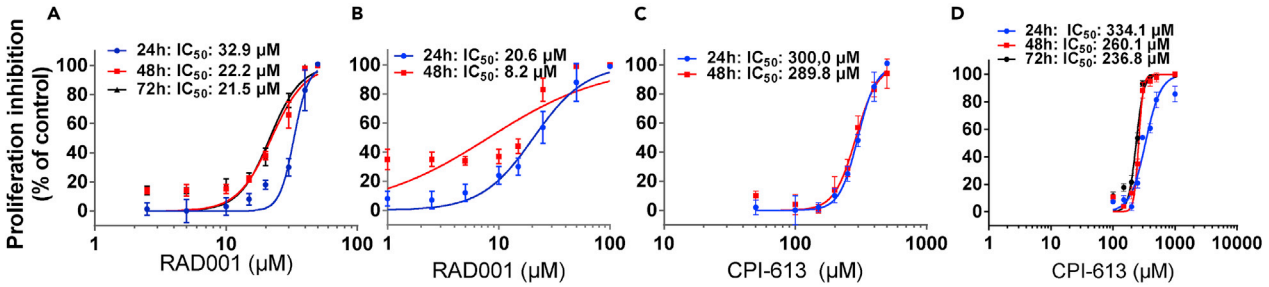

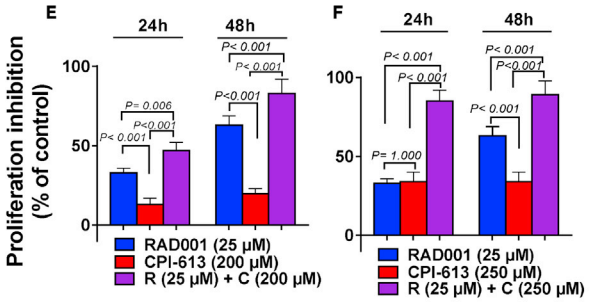

G

BLISS synergy score	5.29	0.83	29.22	13.42
CPI-613 (μM)	200	200	250	250
RAD001 (μM)	25	25	25	25
Duration (h)	24	48	24	48

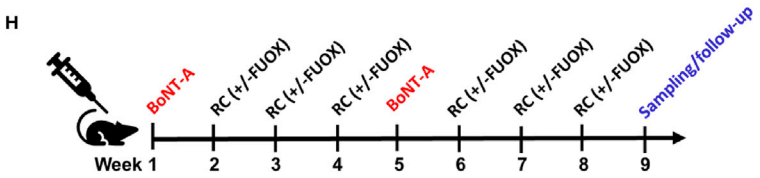

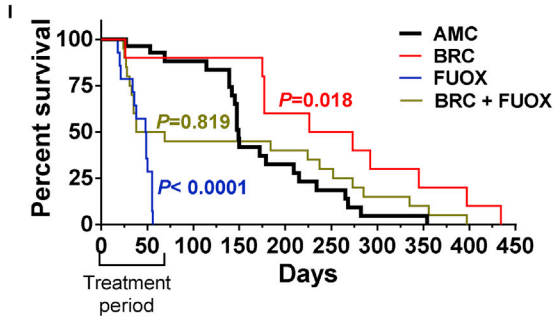

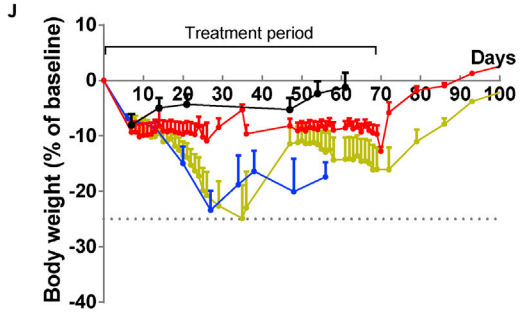

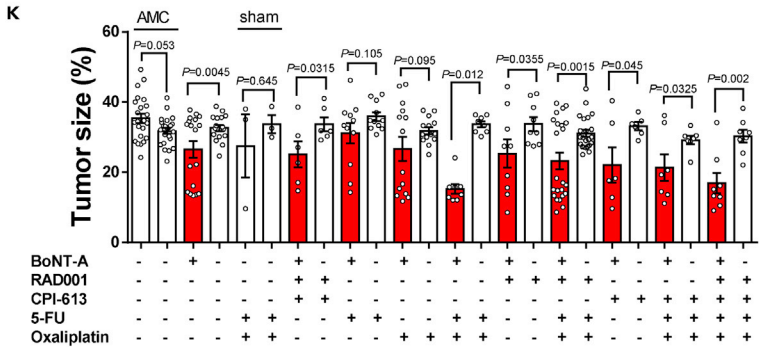

Figure 7. Validation of BRC treatment *in vitro* and *in vivo*

Dose- and time-dependent inhibition of proliferation in response to RAD001 and CPI-613 in MKN74 (A, C) and KATO-III cells (B, D).

Proliferation inhibition of MKN74 cells in response to either RAD001 (25 μM), CPI-613 (200 μM or 250 μM), or combinations at 24–48 h (E-F) with BLISS synergy score for each combination (G).

BLISS score >10 indicates synergistic effect. Mean of n = 3–12 replicates/treatment with SD. Two-way ANOVA between treatments (time x dose).

Proliferation was measured using CCK-8 kit at 450 nm. See also Figures S2 and S4. Timeline for *in vivo* treatment of BoNT-A, RAD001, CPI-613 with and without FUOX over a period of two months (H).

Kaplan-Meier survival curves (I) and body weight change (J) in mouse GC (age 9–15 months) that received more than 1 cycle of treatments of BoNT-A (0.1 U/month) + RAD001 (1.5 mg/kg/day) + CPI-613 (20 mg/kg/week) (BRC), 5-fluorouracil (5 mg/kg/week) + Oxaliplatin (25 mg/kg/week) (FUOX), or BRC + FUOX or no treatment (age-matched control, AMC). Log rank (Mantel-Cox) post hoc test between groups (two-tailed). GraphPad Prism v6.

Tumor size (expressed as volume density in % of glandular area of stomach occupied by tumor) of mouse GC after 2 months treatment with indicated drugs (K). Mean ± SEM with paired t test (AMC: two-tailed, treatments: one-tailed) between anterior (denervated) and posterior (innervated) side of the stomach or non-parametric test as appropriate. Sham: Laparotomy procedure without denervation surgery.

Metabolic gene expression profile in neoplasia is a target site for BRC in clinical trial

Pathogenesis of GC is believed to involve the following cascade: gastritis, atrophy, intestinal metaplasia, dysplasia, and ultimately malignant neoplasms, known as the Correa pathway (Correa, 1992). However, it remains unclear whether metaplasia is a direct precursor of GC, and if so, it should be taken together with neoplasia as targets for treatment of GC (Kinoshita et al., 2017). We have followed-up 17 patients who underwent subtotal or total gastrectomy with radical lymph node dissection, adjuvant chemoradiotherapy, or perioperative chemotherapy for 5 years. We found that patients with high scores of gastric histology activation index (GHAI) had shorter MS than those with low scores, and there was positive correlation between upregulated gene expression and GHAI score and negative correlation between upregulated gene expression profile and OS (Figures 8G–8I). Furthermore, we found distinct expression profiles in signaling pathways in general and the metabolic gene expression profiles in particular between metaplasia and neoplasia (Figures 8J and 8K), suggesting that the two pathological phenotypes harbored distinct metabolic profiles and that the network of the metabolic genes within the neoplasia should be the potential target. These results supported the rationale of BRC clinical trial.

We next carried out a pilot phase II clinical trial (https://clinicaltrials.gov/ct2/show/NCT01822210?term=BoNT-A+and+gastric+cancer&draw=2&rank=1) in which BoNT-A injection was performed through gastroscopy (without systemic administration of RAD001 plus CPI-613). The purpose of this initial clinical trial was to obtain data needed to calculate sample size in a larger controlled trial. Six enrolled patients were diagnosed as gastric adenocarcinomas with locally non-resectable and/or with distant metastasis and lack of response or non-tolerance to second-line chemotherapy (Table S8. Baseline patient data, Related to Figure 8L). We found that the procedure with BoNT-A injections was well tolerated, without any immediate surgical complications or adverse effects. Injections directly into the tumor were associated with a small amount of bleeding from the injection sites, but the bleeding was self-limited and none of the patients required surgical or endoscopic intervention or blood transfusions. We found that the tumor size was reduced during the first 8 weeks and the tumor growth was stabilized afterward in one of three patients (Figure 8L; Table S9. Primary outcome measures, Related to Figure 8L). All patients were without adverse effects or complications and discharged from hospital the first day after the procedure (Tables S10. Secondary outcome measures (short term), Related to Figure 8L; Table S11. Secondary outcome measures (long-term), Related to Figure 8L). Due to aggressive progression at advanced late-stage disease, four out of six patients did not survive until eight weeks after the BoNT-A injection. Two out of six patients were followed for eight weeks and one patient was followed for 20 weeks after receiving BoNT-A treatment. These results suggested that endoscopic injection of BoNT-A could be safe and BRC can be further tested in GC patients that failed second-line chemotherapy.

DISCUSSION

Vagotomy was used extensively in 70s–80s as a surgical treatment for peptic ulcer, due to its inhibitory effects on gastric acid secretion (Rabben et al., 2016). Inhibition of cholinergic signaling has proved to be a possible therapeutic modality (Magnon et al., 2013) and epidemiological, animal, and clinical studies have shown that vagotomy reduces the risk of GC and suppresses gastric tumorigenesis, most likely through muscarinic cholinergic/acetylcholine receptor 3 (M3R)-mediated WNT signaling, proposed as a nerve-cancer crosstalk (Zhao et al., 2014; Hayakawa et al., 2017; Wang et al., 2018).

Cancer cells exhibit a high rate of glycolysis even in the presence of oxygen, the so-called Warburg effect, which has been well recognized as a form of metabolic reprogramming (Hanahan and Weinberg, 2011; Liberti

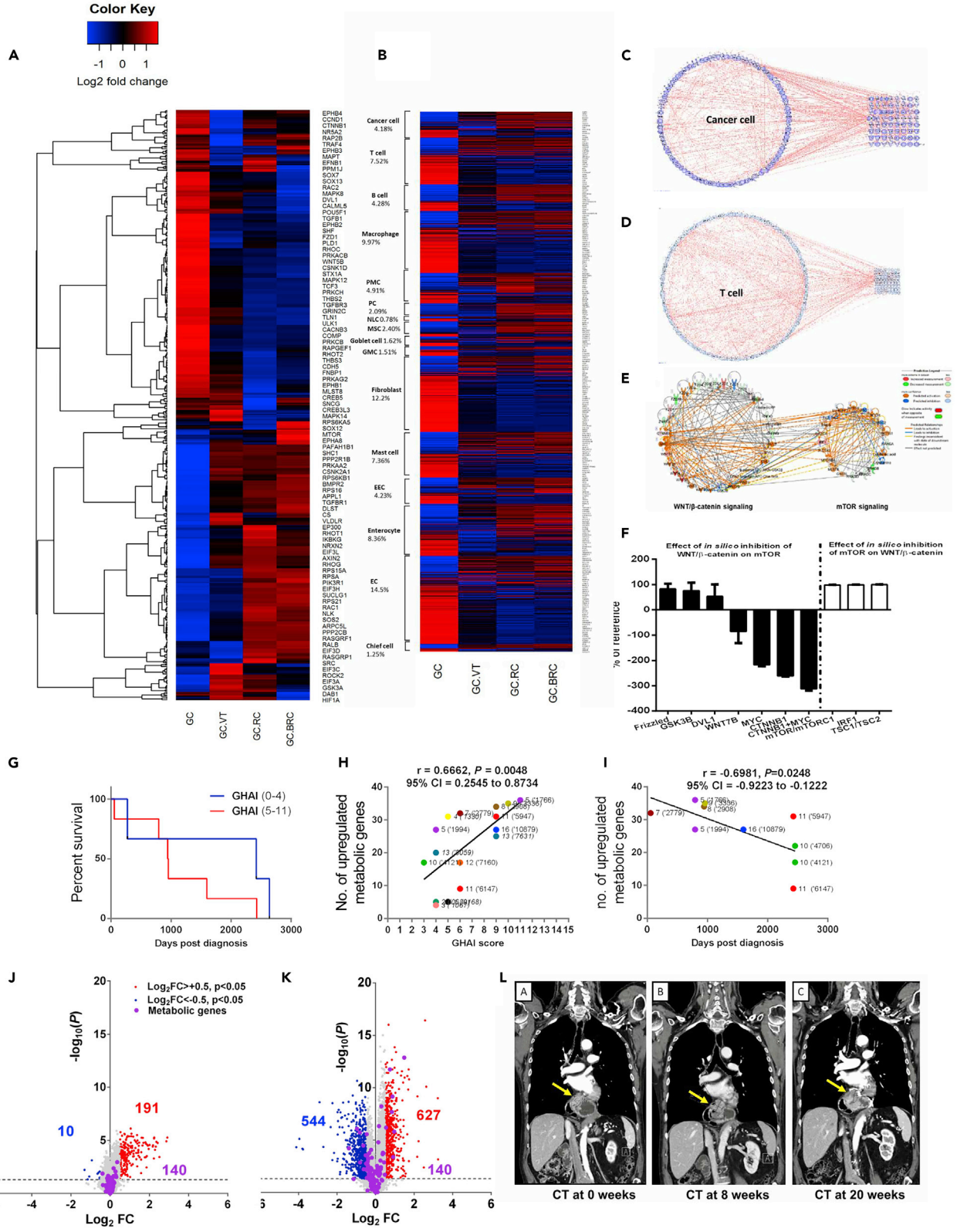
A
Color Key
-1 0 1
Log2 fold change
GC
GC.VT
GC.RC
GC.BRC
B
Cancer cell 4.18%
T cell 7.52%
B cell 4.28%
Macrophage 9.97%
PMC 4.91%
PC 2.09%
NLC 0.78%
MSC 2.40%
Goblet cell 1.62%
GMC 1.51%
Fibroblast 12.2%
Mast cell 7.36%
EEC 4.23%
Enterocyte 8.36%
EC 14.5%
Chief cell 1.25%
C
Cancer cell
D
T cell
E
WNT/β-catenin signaling
mTOR signaling
F
Effect of in silico inhibition of WNT/β-catenin on mTOR
Effect of in silico inhibition of mTOR on WNT/β-catenin
% of reference
Frizzled
GSK3B
DVL1
WNT7B
MYC
CTNNB1:MYC
mTOR/mTORC1
IRF1
TSC1/TSC2
G
GHAI (0-4)
GHAI (5-11)
Percent survival
Days post diagnosis
H
r = 0.6662, P = 0.0048
95% CI = 0.2545 to 0.8734
No. of upregulated metabolic genes
GHAI score
I
r = -0.6981, P=0.0248
95% CI = -0.9223 to -0.1222
no. of upregulated metabolic genes
Days post diagnosis
J
Log2FC>+0.5, p<0.05
Log2FC<-0.5, p<0.05
Metabolic genes
-log10(P)
191
10
140
Log2 FC
K
-log10(P)
544
627
140
Log2 FC
L
A
B
C
CT at 0 weeks
CT at 8 weeks
CT at 20 weeks

Figure 8. Transcriptome profiling of nerve-cancer metabolism pathways and cellular compartments, computational network modeling, *in silico* testing, clinical analysis, and trial in GC

Heatmap of the gene expression profile of pathways including WNT/β-catenin signaling, mTOR signaling, synaptogenesis pathway, and TCA cycle in mouse gastric cancer (GC), GC after VT, RC, or BRC (A). See also Figure S5.

Heatmap of the single-cell transcriptome atlas in mouse GC, GC after VT, RC, or BRC (B). The expression levels of marker genes were analyzed in mouse GC versus WT for each representative cell type according to the single-cell atlas (Zhang et al., 2019, PMID: 31067475, GSE134520). EC, endothelial cell; GMC, antral basal gland mucous cell; EEC, enteroendocrine cell; MSC, metaplastic stem-like cell; PC, proliferative cell; PMC, pit mucous cell; NLC, neck-like cell. Percentages of total number of genes in each cell type are displayed under each cell name (smooth muscle cell not included). Gene expression on $\log_2$ fold scale; blue: downregulated; red: upregulated.

Heatmaps in A–B created in RStudio version 3.5.2 using heatmap.2-function. Computational network modeling (IPA) showing interactions within cancer cell gene cluster (C) and T cell gene cluster (D) and connections between the cell type-specific genes and genes involved in WNT/mTOR/glutaminolysis (C,D). See also Figure S6. *In silico* modeling showing WNT/β-catenin signaling (left) and mTOR signaling (right) clusters of mouse GC utilizing the MAP function in IPA (E).

In silico data inhibition to predict effects of inhibition of WNT/β-catenin signaling pathway intermediates on mTOR network cluster (F, black bars) and *vice versa* (F, white bars). Percentages (in F) are calculated based on semi-quantitative reference values derived from predicted downstream effects generated in IPA. Means of n = 7–14 *in silico* tests/group.

See also Figure S7. Kaplan-Meier survival curves of 17 gastric cancer (GC) patients with low GHAI score (0–4, MS: 2420 days) and high GHAI score (5–11, MS: 949.5 days) (G).

Correlation of number of upregulated metabolic genes in patients diagnosed with gastric adenocarcinoma versus GHAI score (H), and correlation of number of upregulated metabolic genes (corresponding to Figure 2) in patients diagnosed with gastric adenocarcinoma versus survival days (I).

Note: metabolic genes are the same as in Figures 2A–2C. Volcano plots of global gene expression profiles in metaplasia (J) and neoplasia (K) in GC patients. Metabolic genes and interactions are highlighted according to regulation status (blue: downregulated; red: upregulated). Note: metabolic genes are the same as presented in Figures 2A–2C and Data S2. Tumor growth was stabilized after 20 weeks post-BoNT-A endoscopic injection in one patient as shown by CT scan (L).

and Locasale, 2016; Schulze and Harris, 2012; Lunt and Vander Heiden, 2011). In line with our recent understanding of tumor heterogeneity, it seems unlikely that there exists a common "metabolic reprogramming" that describes all cancer cell types and/or tumor types (including both cancer cells and TME) (Cluntun et al., 2017). It has been a dogma that GC is associated with the Warburg effect (Vander Heiden et al., 2009). In the present study, we found that the mouse GC model was well representative of human GC, particularly regarding the metabolic reprogramming, which was not associated with the Warburg effect. By comparisons between WT versus GC mice, which also included a comparison of the innervated side versus denervated sides of the same stomach of WT or GC mice, we found that inhibition of glutaminolysis and restoration of OXPHOS/glycolysis after vagotomy were the likely mechanisms underlying vagotomy-induced suppression of GC tumorigenesis. Thus, the lack of glycolytic metabolite elevations, along with a notable increase of glutaminolytic metabolites and inactivated AMPK signaling in the mouse GC model, led us to suggest that GC is glutamine dependent rather than glucose dependent, given the fact that AMPK signaling is considered to be a demand-driven regulator of glucose uptake and glycolysis (Ye and Medzhitov, 2019). This was in line with previous reports in several other cancer types including triple negative breast cancer (Sherwood et al., 2014; Sethi and Vidal-Puig, 2010; Li and Zhang, 2016; Minkler et al., 2005; Berg et al., 2002). This was also in line with reports of fluorine 18-fluorodeoxyglucose positron tomography (FDG-PET) for GC patients showing a limited value in diagnosis and evaluation, as it is designed based on increased glucose metabolism in tumor (Morgagni et al., 2020; Matzinger et al., 2009; Sprinz et al., 2018).

Through a multi-omics approach, we identified common signaling pathways that were shared between transcriptomics and metabolomics analyses. We found that among nerve-related signaling pathways, synaptogenesis signaling pathway was activated in GC and inhibited after vagotomy. This signaling pathway consists of several components involved with the nerve-cancer axis, including WNT signaling-related molecules, neurexins, neuroligins, EphB, and Trk receptors (Biederer and Stagi, 2008; Rosso et al., 2013). By transcriptomics analysis, we found that vagotomy inhibited WNT/β-catenin signaling and mTOR signaling. The WNT/β-catenin signaling pathway has been demonstrated to play prominent roles during embryonic development and adult tissue homeostasis by maintaining somatic stem cell functions (Fu et al., 2013). The mTORC1 signaling pathway has also been implicated in regulating stem cell functions in multiple tissue types (Zoncu et al., 2011). In homeostatic conditions, these pathways show a fine regulation through feedback mechanisms and are connected at multiple levels involving both upstream and downstream common effectors. For instance, activation of mTORC1 signaling could lead to suppression of WNT/β-catenin signaling through downregulating the FZD level in normal mouse intestines (Zeng et al., 2018). However, the interconnection (or feedback loop) between these two signaling pathways could be dysregulated in the case of cancer. The results of the present study suggested that the WNT/β-catenin signaling regulated the mTOR pathway in GC and might be an upstream driver of the mTOR pathway in GC. Both pathways

were suppressed by vagotomy in GC and even more so by RAD001 (inhibition of mTOR) and CPI-613 (inhibition of PDH and α-KGDH). This is in line with the hypothesis that cancer is driven by dysregulated WNT/β-catenin signaling, and the relationship between WNT/β-catenin and mTORC1 pathways is so close that they should be considered as a unique therapeutic target (Prossomariti et al., 2020).

The phenotype of gastric tissue after vagotomy in GC mice appeared to be "normal" in terms of histology (Zhao et al., 2014) and metabolic profile (this study), which was associated with the signaling pathways such as the TCA cycle, protein kinase A signaling, calcium signaling, gap junction signaling, and phospholipases. Thus, these signaling pathways presented in "normalized" tissues would likely not be considered as potential therapeutic targets. Using a network integration approach for drug-target interaction prediction and computational drug repositioning, we predicted that targeting mTOR with RAD001 (everolimus), PDP1/α-KGDH with CPI-613, and SNAP25 with BoNT-A as BRC therapy would inhibit the downstream factors of signaling pathways including proteins, microRNA, and metabolites and lead to therapeutic outcomes. Indeed, the results of the present study showed that the therapeutic effects of either RC or BRC were associated with downregulation of glutaminolysis-WNT-mTOR-c-MYC signaling pathway in the cancer cells as well as the TME. It should be noticed that the metabolic reprogramming took place in the neoplasia but not in the metaplasia in patients, supporting that (1) the metabolic reprogramming is reflected by cancer cells as well as TME; (2) that the metabolic properties evolve during tumor progression, and (3) that the site of neoplasia is ideal location for injection of BoNT-A.

Recent findings in immunometabolism have shown that the effects of cancer cell metabolism on the TME may involve direct modulation of essential T cell metabolic pathways and activities and suggested a "metabolic checkpoint" for tumor immunotherapy, in which effector T cells responded to glutamine antagonism by markedly upregulating oxidative metabolism and adopting a long-lived, highly activated phenotype (Leone et al., 2019). It was also reported that inhibiting glutamine metabolism of myeloid-derived suppressor cells (MDSCs) led to activation-induced cell death and conversion of MDSCs to inflammatory macrophages and suggested that myeloid cells comprised a major component of TME, promoting tumor growth and immune evasion (Oh et al., 2020). The success of immunotherapy in GC has to date been limited in part by the lack of knowledge on gastric-specific TME (Subhash et al., 2015). A recent study showed that a gastric-specific TME atlas consisted of the gene expression pattern in connection with a variety of resident and infiltrating host cells (such as endothelial cells, enterocytes, chief cells, antral basal gland cells, metaplastic stem-like cells, pit mucous cells, enteroendocrine cells, fibroblasts, T cells, B cells, mast cells, and microphages) (Zhang et al., 2019). According to the atlas, the results of the present study further showed that the gene expression of immune/inflammatory cells, such as T cells, B cells, macrophages, and mast cells in TME of GC was reversed together with the metabolic reprogramming after vagotomy or RC or BRC. Presumably, the therapeutic strategy should be to enhance the robustness of GC immunotherapy by the "nerve-cancer metabolism therapy" that was presented in the present study.

GC accounts for the third highest cancer-related disability-adjusted life-years (DALYs) after lung and liver cancers (Collaborators, 2020), in addition to its high incidence and mortality. Although *H. pylori* infection is declining, the trends toward increased obesity and aging of the population will likely result in a continued high incidence of GC. Thus, less invasive and better tolerated therapies need to be developed for the treatment of elderly patients with GC. Based on the successful progress in the treatment of gastric cancer in Japan over the last 50 years, it was suggested that endoscopic submucosal dissection (ESD) combined with "gentler" chemotherapy or immunotherapy could be applied to more than half of the GC patients (Sasako, 2020). The results of the present study indicated that endoscopic submucosal/intratumoral injection of BoNT-A combined with non-cytotoxic chemotherapy could be an ideal therapy for the elderly patients. In the present study, we choose the non-cytotoxic drugs, RAD001 (also known as everolimus) and CPI-613 (also known as devimistat), as they have been well tested in clinical trials for other types of cancer (Kim et al., 2017, 2018; Chung et al., 2016; Pardee et al., 2018; Alistar et al., 2017).

In addition to GC, nerve-cancer crosstalk takes place in other types of cancer, e.g. prostate cancer, colorectal cancer, pancreatic cancer, and breast cancer (Chen and Ayala, 2018; Zahalka et al., 2017; Renz et al., 2018; Dubeykovskaya et al., 2016; Kamiya et al., 2019; Mauffrey et al., 2019). More studies are needed to investigate the underlying mechanisms, along with the metabolic reprogramming and immunometabolism, and to develop the nerve-cancer metabolism therapy.

In conclusion, the nature of the present study was translational in order to develop new treatment that is closely linked with clinical trials. Based on the results of the present study, we suggested that GC (including both the cancer cells and TME) was glutamine dependent with altered neuronal and metabolic signaling pathways; vagotomy and metabolic inhibitors reversed the metabolic reprogramming in GC; WNT-mTOR signaling pathway played an important role in the metabolic switch between oxidative phosphorylation/glycolysis and glutaminolysis in GC; SNAP25, mTOR, PDP1/α-KGDH, and glutaminolysis were potential drug-targets for treatment of GC; and intratumoral injection of BoNT-A with systemic administration of RAD001(everolimus) and CPI-613 (devimistat) can be a potential therapy for GC. The potential therapy was particular for elderly patients with clinical endpoints of increased OS and QoF, which have been established according to the regulation of European Commission. The treatment methods used in the present study were commonly considered having no/little stress and abdominal pain, i.e. injections of BoNT-A (through gastroscopy in patients and laparotomy in mice) and RAD001 and CPI-613 (i.v. in patients and i.p. in mice). In the present study, the long-term follow-up (14 months after starting treatment in mice) showed that OS was 33% without any treatment, 40% with chemotherapy (cytotoxic drugs), but 90% with the new treatment (without cytotoxic drugs).

Limitations of the study

The so-called "metabolic escape" has been suggested as a mechanism by cancer cells to avoid cell death in response to inhibited glutaminolysis. Thus, tumors that suffer from glucose/glutamine starvation frequently activate fatty acid catabolism for survival (Halama et al., 2018; Wise et al., 2008; Li and Zhang, 2016). The results of the present study might suggest that the metabolic escape takes place after vagotomy, leading to an activation of Acetyl-CoA with increased levels of lysolipids and polyunsaturated fatty acids in GC but not in WT mice. Furthermore, acyl carnitine oleoylcarnitine, a long-chain acyl carnitine that accumulates during certain metabolic conditions, such as fasting and nutrient deficiency (Minkler et al., 2005), was increased after vagotomy along with its transporter SLC25A20, probably supporting the notion that acyl carnitines serves to deliver fatty acids to the mitochondria for β-oxidation to produce acetyl-CoA (Berg et al., 2002). Monoacylglycerol 1-stearoylglycerol (1-monostearin) was increased after vagotomy in GC but not in WT mice, probably further suggesting that vagotomy-induced suppression of tumorigenesis was mediated in part through accelerated degradation of diacyl- or triacylglyserols, as well as deoxycarnitine, succinylcarnitine, and 3-dehydrocarnitine. These assumptions need to be further investigated.

Resource availability

Lead contact

Information and requests for resources should be directed to and will be fulfilled by the Lead Contact, Chun-Mei Zhao (chun-mei.zhao@ntnu.no).

Materials availability

This study did not generate new unique reagents.

Data and code availability

All relevant data are available from the Lead Contact upon request. The mouse RNA seq/microarray data (related to Data S1–S3) have been deposited in the NCBI Bioproject database under the accession number PRJNA690520, which can be accessed using the following link: http://www.ncbi.nlm.nih.gov/bioproject/690520, and in the GEO under accession number GSE30295, respectively. The human microarray data (related to Data S1 and S2) are available online via Mendeley Data repository with DOI link at https://doi.org/10.17632/hzmfshy7hp.1.

METHODS

All methods can be found in the accompanying Transparent methods supplemental file.

SUPPLEMENTAL INFORMATION

Supplemental Information can be found online at https://doi.org/10.1016/j.isci.2021.102091.

ACKNOWLEDGMENTS

The authors thank the grant supports by the Liaison Committee between the Central Norway Regional Health Authority (Helse-Midt Norge RHF) and Norwegian University of Science and Technology (NTNU),

Norway (grant numbers 46056636/46056928/90061700/90061701), Joint Program of the Medical Faculty of NTNU and St. Olavs University Hospital, the Cancer Foundation of St. Olavs Hospital (Kreftfondet ved St. Olavs hospital), and the technical support by Genomics Core Facility (GCF), which is funded by the Faculty of Medicine and Health Sciences at NTNU and RHF.

AUTHORS CONTRIBUTION

H-L.R. and G.T.A.: *in vitro*, *in vivo*, and *in silico* experiments, sample/data collection and preparation, data analysis and interpretation, writing manuscript. M.K.O.: *in vivo*, experiments, writing manuscript. A.I. and D.K.: data visualization and drug synergy prediction, writing manuscript. A.Ø.: *in vitro* experiments, writing manuscript. T.C.W.: data acquisitioning, writing manuscript. S.L.: clinical interpretation, writing manuscript. J.E.G.: clinical samples and data collection, writing manuscript. D.C.: project concept, study idea and design, data analysis and interpretation, writing manuscript. C-M.Z.: project concept, study idea and design, lab and clinical experiments, data interpretation, writing manuscript.

DECLARATION OF INTERESTS

The authors declare no competing interests.

Received: September 2, 2020
Revised: November 23, 2020
Accepted: January 18, 2021
Published: February 19, 2021

REFERENCES

Alistar, A., Morris, B.B., Desnoyer, R., Klepin, H.D., Hosseinzadeh, K., Clark, C., Cameron, A., Leyendecker, J., D'agostino, R., Jr., Topaloglu, U., et al. (2017). Safety and tolerability of the first-in-class agent CPI-613 in combination with modified FOLFIRINOX in patients with metastatic pancreatic cancer: a single-centre, open-label, dose-escalation, phase 1 trial. Lancet Oncol. *18*, 770–778.

Berg, J.M., Tymoczko, J.L., and Stryer, L. (2002). Biochemistry: The Utilization of Fatty Acids as Fuel Requires Three Stages of Processing (W.H.Freeman & Co Ltd).

Biederer, T., and Stagi, M. (2008). Signaling by synaptogenic molecules. Curr. Opin. Neurobiol. *18*, 261–269.

Chen, D., and Ayala, G.E. (2018). Innervating prostate cancer. N. Engl. J. Med. *378*, 675–677.

Chung, V., Frankel, P., Lim, D., Yeon, C., Leong, L., Chao, J., Ruel, N., Luevanos, E., Koehler, S., Chung, S., et al. (2016). Phase Ib trial of mFOLFOX6 and everolimus (NSC-733504) in patients with metastatic gastroesophageal adenocarcinoma. Oncology *90*, 307–312.

Cluntun, A.A., Lukey, M.J., Cerione, R.A., and Locasale, J.W. (2017). Glutamine metabolism in cancer: understanding the heterogeneity. Trends Cancer *3*, 169–180.

Collaborators, G.B.D.S.C. (2020). The global, regional, and national burden of stomach cancer in 195 countries, 1990-2017: a systematic analysis for the Global Burden of Disease study 2017. Lancet Gastroenterol. Hepatol. *5*, 42–54.

Coller, H.A. (2014). Is cancer a metabolic disease? Am. J. Pathol. *184*, 4–17.

Correa, P. (1992). Human gastric carcinogenesis: a multistep and multifactorial process–first American cancer society award lecture on cancer epidemiology and prevention. Cancer Res. *52*, 6735–6740.

Deberardinis, R.J., and Chandel, N.S. (2016). Fundamentals of cancer metabolism. Sci. Adv. *2*, e1600200.

Dorsam, B., and Fahrer, J. (2016). The disulfide compound alpha-lipoic acid and its derivatives: a novel class of anticancer agents targeting mitochondria. Cancer Lett. *371*, 12–19.

Dressler, D., Saberi, F.A., and Barbosa, E.R. (2005). Botulinum toxin: mechanisms of action. Arq Neuropsiquiatr *63*, 180–185.

Dubeykovskaya, Z., Si, Y., Chen, X., Worthley, D.L., Renz, B.W., Urbanska, A.M., Hayakawa, Y., Xu, T., Westphalen, C.B., Dubeykovskiy, A., et al. (2016). Neural innervation stimulates splenic TFF2 to arrest myeloid cell expansion and cancer. Nat. Commun. *7*, 10517.

Duran, R.V., Oppliger, W., Robitaille, A.M., Heiserich, L., Skendaj, R., Gottlieb, E., and Hall, M.N. (2012). Glutaminolysis activates Rag-mTORC1 signaling. Mol. Cell *47*, 349–358.

Faivre, S., Kroemer, G., and Raymond, E. (2006). Current development of mTOR inhibitors as anticancer agents. Nat. Rev. Drug Discov. *5*, 671–688.

Fox, J.G., and Wang, T.C. (2007). Inflammation, atrophy, and gastric cancer. J. Clin. Invest. *117*, 60–69.

Fu, Y., Huang, B., Shi, Z., Han, J., Wang, Y., Huangfu, J., and Wu, W. (2013). SRSF1 and SRSF9 RNA binding proteins promote Wnt signalling-mediated tumorigenesis by enhancing beta-catenin biosynthesis. EMBO Mol. Med. *5*, 737–750.

Fung, M.K.L., and Chan, G.C.-F. (2017). Drug-induced amino acid deprivation as strategy for cancer therapy. J. Hematol. Oncol. *10*, 144.

Grigoryan, T., Stein, S., Qi, J., Wende, H., Garratt, A.N., Nave, K.A., Birchmeier, C., and Birchmeier, W. (2013). Wnt/Rspondin/beta-catenin signals control axonal sorting and lineage progression in Schwann cell development. Proc. Natl. Acad. Sci. U S A *110*, 18174–18179.

Halama, A., Kulinski, M., Dib, S.S., Zaghlool, S.B., Siveen, K.S., Iskandarani, A., Zierer, J., Prabhu, K.S., Satheesh, N.J., Bhagwat, A.M., et al. (2018). Accelerated lipid catabolism and autophagy are cancer survival mechanisms under inhibited glutaminolysis. Cancer Lett. *430*, 133–147.

Hanahan, D., and Weinberg, R.A. (2011). Hallmarks of cancer: the next generation. Cell *144*, 646–674.

Hayakawa, Y., Sakitani, K., Konishi, M., Asfaha, S., Niikura, R., Tomita, H., Renz, B.W., Tailor, Y., Macchini, M., Middelhoff, M., et al. (2017). Nerve growth factor promotes gastric tumorigenesis through aberrant cholinergic signaling. Cancer Cell *31*, 21–34.

Hirayama, A., Kami, K., Sugimoto, M., Sugawara, M., Toki, N., Onozuka, H., Kinoshita, T., Saito, N., Ochiai, A., Tomita, M., et al. (2009). Quantitative metabolome profiling of colon and stomach cancer microenvironment by capillary electrophoresis time-of-flight mass spectrometry. Cancer Res. *69*, 4918–4925.

Jobling, P., Pundavela, J., Oliveira, S.M., Roselli, S., Walker, M.M., and Hondermarck, H. (2015). Nerve-cancer cell cross-talk: a novel promoter of tumor progression. Cancer Res. *75*, 1777–1781.

Kahn, M. (2014). Can we safely target the WNT pathway? Nat. Rev. Drug Discov. *13*, 513–532.

Kamiya, A., Hayama, Y., Kato, S., Shimomura, A., Shimomura, T., Irie, K., Kaneko, R., Yanagawa, Y., Kobayashi, K., and Ochiya, T. (2019). Genetic manipulation of autonomic nerve fiber innervation and activity and its effect on breast cancer progression. Nat. Neurosci. *22*, 1289–1305.

Kim, H.S., Shaib, W.L., Zhang, C., Nagaraju, G.P., Wu, C., Alese, O.B., Chen, Z., Brutcher, E., Renfroe, M., and El-Rayes, B.F. (2018). Phase 1b study of pasireotide, everolimus, and selective internal radioembolization therapy for unresectable neuroendocrine tumors with hepatic metastases. Cancer *124*, 1992–2000.

Kim, S.T., Lee, J., Park, S.H., Park, J.O., Park, Y.S., Kang, W.K., and Lim, H.Y. (2017). Prospective phase II trial of everolimus in PIK3CA amplification/mutation and/or PTEN loss patients with advanced solid tumors refractory to standard therapy. BMC Cancer *17*, 211.

Kinoshita, H., Hayakawa, Y., and Koike, K. (2017). Metaplasia in the stomach-precursor of gastric cancer? Int. J. Mol. Sci. *18*, 2063.

Lee, K.C., Maturo, C., Perera, C.N., Luddy, J., Rodriguez, R., and Shorr, R. (2014). Translational assessment of mitochondrial dysfunction of pancreatic cancer from in vitro gene microarray and animal efficacy studies, to early clinical studies, via the novel tumor-specific anti-mitochondrial agent, CPI-613. Ann. Transl Med. *2*, 91.

Leone, R.D., Zhao, L., Englert, J.M., Sun, I.M., Oh, M.H., Sun, I.H., Arwood, M.L., Bettencourt, I.A., Patel, C.H., Wen, J., et al. (2019). Glutamine blockade induces divergent metabolic programs to overcome tumor immune evasion. Science *366*, 1013–1021.

Li, Z., and Zhang, H. (2016). Reprogramming of glucose, fatty acid and amino acid metabolism for cancer progression. Cell Mol. Life Sci. *73*, 377–392.

Liao, G.Y., Lee, M.T., Fan, J.J., Hsiao, P.W., Lee, C.S., Su, S.Y., Hwang, J.J., and Ke, F.C. (2019). Blockage of glutamine-dependent anaplerosis affects mTORC1/2 activity and ultimately leads to cellular senescence-like response. Biol. Open *8*, bio038257.

Liberti, M.V., and Locasale, J.W. (2016). The Warburg effect: how does it benefit cancer cells? Trends Biochem. Sci. *41*, 211–218.

Loponte, S., Lovisa, S., Deem, A.K., Carugo, A., and Viale, A. (2019). The many facets of tumor heterogeneity: is metabolism lagging behind? Cancers (Basel) *11*, 1574.

Lunt, S.Y., and Vander Heiden, M.G. (2011). Aerobic glycolysis: meeting the metabolic requirements of cell proliferation. Annu. Rev. Cell Dev. Biol. *27*, 441–464.

Magnon, C., Hall, S.J., Lin, J., Xue, X., Gerber, L., Freedland, S.J., and Frenette, P.S. (2013). Autonomic nerve development contributes to prostate cancer progression. Science *341*, 1236361.

Matsuda, T., and Saika, K. (2013). The 5-year relative survival rate of stomach cancer in the USA, Europe and Japan. Jpn. J. Clin. Oncol. *43*, 1157–1158.

Matzinger, O., Gerber, E., Bernstein, Z., Maingon, P., Haustermans, K., Bosset, J.F., Gulyban, A., Poortmans, P., Collette, L., and Kuten, A. (2009). EORTC-ROG expert opinion: radiotherapy volume and treatment guidelines for neoadjuvant radiation of adenocarcinomas of the gastroesophageal junction and the stomach. Radiother. Oncol. *92*, 164–175.

Mauffrey, P., Tchitchek, N., Barroca, V., Bemelmans, A., Firlej, V., Allory, Y., Romeo, P.H., and Magnon, C. (2019). Progenitors from the central nervous system drive neurogenesis in cancer. Nature *569*, 672–678.

Minkler, P.E., Kerner, J., North, K.N., and Hoppel, C.L. (2005). Quantitation of long-chain acylcarnitines by HPLC/fluorescence detection: application to plasma and tissue specimens from patients with carnitine palmitoyltransferase-II deficiency. Clin. Chim. Acta *352*, 81–92.

Morgagni, P., Bencivenga, M., Colciago, E., Tringali, D., Giacopuzzi, S., Framarini, M., Saragoni, L., Mura, G., Graziosi, L., Marino, E., et al. (2020). Limited usefulness of 18F-FDG PET/CT in predicting tumor regression after preoperative chemotherapy for noncardia gastric cancer: the Italian research group for gastric cancer (GIRCG) experience. Clin. Nucl. Med. *45*, 177–181.

Naumann, M., and Jankovic, J. (2004). Safety of botulinum toxin type A: a systematic review and meta-analysis. Curr. Med. Res. Opin. *20*, 981–990.

Oh, M.H., Sun, I.H., Zhao, L., Leone, R.D., Sun, I.M., Xu, W., Collins, S.L., Tam, A.J., Blosser, R.L., Patel, C.H., et al. (2020). Targeting glutamine metabolism enhances tumor specific immunity by modulating suppressive myeloid cells. J. Clin. Invest. *130*, 3865–3884.

Pardee, T.S., Anderson, R.G., Pladna, K.M., Isom, S., Ghiraldeli, L.P., Miller, L.D., Chou, J.W., Jin, G., Zhang, W., Ellis, L.R., et al. (2018). A phase I study of CPI-613 in combination with high-dose cytarabine and mitoxantrone for relapsed or refractory acute myeloid leukemia. Clin. Cancer Res. *24*, 2060–2073.

Pardee, T.S., Lee, K., Luddy, J., Maturo, C., Rodriguez, R., Isom, S., Miller, L.D., Stadelman, K.M., Levitan, D., Hurd, D., et al. (2014). A phase I study of the first-in-class antimitochondrial metabolism agent, CPI-613, in patients with advanced hematologic malignancies. Clin. Cancer Res. *20*, 5255–5264.

Parkin, D.M., Bray, F., Ferlay, J., and Pisani, P. (2005). Global cancer statistics, 2002. CA Cancer J. Clin. *55*, 74–108.

Pavlova, N.N., and Thompson, C.B. (2016). The emerging hallmarks of cancer metabolism. Cell Metab. *23*, 27–47.

Prossomariti, A., Piazzi, G., Alquati, C., and Ricciardiello, L. (2020). Are Wnt/beta-catenin and PI3K/AKT/mTORC1 distinct pathways in colorectal cancer? Cell Mol. Gastroenterol. Hepatol. *10*, 491–506.

Rabben, H.L., Zhao, C.M., Hayakawa, Y., Wang, T.C., and Chen, D. (2016). Vagotomy and gastric tumorigenesis. Curr. Neuropharmacol. *14*, 967–972.

Rawla, P., and Barsouk, A. (2019). Epidemiology of gastric cancer: global trends, risk factors and prevention. Prz Gastroenterol. *14*, 26–38.

Renz, B.W., Takahashi, R., Tanaka, T., Macchini, M., Hayakawa, Y., Dantes, Z., Maurer, H.C., Chen, X., Jiang, Z., Westphalen, C.B., et al. (2018). beta2 adrenergic-neurotrophin feedforward loop promotes pancreatic cancer. Cancer Cell *33*, 75–90.e7.

Rosso, S., Inestrosa, N., and Rosso, S. (2013). WNT signaling in neuronal maturation and synaptogenesis. Front. Cell Neurosci. *7*, 103.

Sanderson, S.M., Gao, X., Dai, Z., and Locasale, J.W. (2019). Methionine metabolism in health and cancer: a nexus of diet and precision medicine. Nat. Rev. Cancer *19*, 625–637.

Sasako, M. (2020). Progress in the treatment of gastric cancer in Japan over the last 50 years. Ann. Gastroenterol. Surg. *4*, 21–29.

Schulze, A., and Harris, A.L. (2012). How cancer metabolism is tuned for proliferation and vulnerable to disruption. Nature *491*, 364–373.

Sethi, J.K., and Vidal-Puig, A. (2010). Wnt signalling and the control of cellular metabolism. Biochem. J. *427*, 1–17.

Seyfried, T.N., Flores, R.E., Poff, A.M., and D'agostino, D.P. (2014). Cancer as a metabolic disease: implications for novel therapeutics. Carcinogenesis *35*, 515–527.

Sherwood, V., Chaurasiya, S.K., Ekstrom, E.J., Guilmain, W., Liu, Q., Koeck, T., Brown, K., Hansson, K., Agnarsdottir, M., Bergqvist, M., et al. (2014). WNT5A-mediated beta-catenin-independent signalling is a novel regulator of cancer cell metabolism. Carcinogenesis *35*, 784–794.

Shimobayashi, M., and Hall, M.N. (2014). Making new contacts: the mTOR network in metabolism and signalling crosstalk. Nat. Rev. Mol. Cell Biol. *15*, 155–162.

Smith, R.L., Soeters, M.R., Wüst, R.C.I., and Houtkooper, R.H. (2018). Metabolic flexibility as an adaptation to energy resources and requirements in health and disease. Endocr. Rev. *39*, 489–517.

Sprinz, C., Altmayer, S., Zanon, M., Watte, G., Irion, K., Marchiori, E., and Hochhegger, B. (2018). Effects of blood glucose level on 18F-FDG uptake for PET/CT in normal organs: a systematic review. PLoS One *13*, e0193140.

Stuart, S.D., Schauble, A., Gupta, S., Kennedy, A.D., Keppler, B.R., Bingham, P.M., and Zachar, Z. (2014). A strategically designed small molecule attacks alpha-ketoglutarate dehydrogenase in tumor cells through a redox process. Cancer Metab. *2*, 4.

Subhash, V.V., Yeo, M.S., Tan, W.L., and Yong, W.P. (2015). Strategies and advancements in harnessing the immune system for gastric cancer immunotherapy. J. Immunol. Res. *2015*, 308574.

Uefuji, K., Ichikura, T., and Mochizuki, H. (2000). Cyclooxygenase-2 expression is related to prostaglandin biosynthesis and angiogenesis in human gastric cancer. Clin. Cancer Res. *6*, 135–138.

Vander Heiden, M.G., Cantley, L.C., and Thompson, C.B. (2009). Understanding the Warburg effect: the metabolic requirements of cell proliferation. Science *324*, 1029–1033.

Vander Heiden, M.G., and Deberardinis, R.J. (2017). Understanding the intersections between metabolism and cancer biology. Cell *168*, 657–669.

Wang, D., and Dubois, R.N. (2018). Role of prostanoids in gastrointestinal cancer. J. Clin. Invest. *128*, 2732–2742.

Wang, L., Xu, J., Xia, Y., Yin, K., Li, Z., Li, B., Wang, W., Xu, H., Yang, L., and Xu, Z. (2018). Muscarinic acetylcholine receptor 3 mediates vagus nerve-induced gastric cancer. Oncogenesis *7*, 88.

Wang, T.C., Koh, T.J., Varro, A., Cahill, R.J., Dangler, C.A., Fox, J.G., and Dockray, G.J. (1996). Processing and proliferative effects of human progastrin in transgenic mice. J. Clin. Invest. *98*, 1918–1929.

Whiteside, T.L. (2008). The tumor microenvironment and its role in promoting tumor growth. Oncogene *27*, 5904–5912.

Wise, D.R., Deberardinis, R.J., Mancuso, A., Sayed, N., Zhang, X.Y., Pfeiffer, H.K., Nissim, I., Daikhin, E., Yudkoff, M., Mcmahon, S.B., et al. (2008). Myc regulates a transcriptional program that stimulates mitochondrial glutaminolysis and leads to glutamine addiction. Proc. Natl. Acad. Sci. U S A *105*, 18782–18787.

Wishart, D.S. (2015). Is cancer a genetic disease or a metabolic disease? EBioMedicine *2*, 478–479.

Ye, J., and Medzhitov, R. (2019). Control strategies in systemic metabolism. Nat. Metab. *1*, 947–957.

Yoshida, G.J. (2015). Metabolic reprogramming: the emerging concept and associated therapeutic strategies. J. Exp. Clin. Cancer Res. *34*, 111.

Zachar, Z., Marecek, J., Maturo, C., Gupta, S., Stuart, S.D., Howell, K., Schauble, A., Lem, J., Piramzadian, A., Karnik, S., et al. (2011). Non-redox-active lipoate derivates disrupt cancer cell mitochondrial metabolism and are potent anticancer agents in vivo. J. Mol. Med. (Berl) *89*, 1137–1148.

Zahalka, A.H., Arnal-Estape, A., Maryanovich, M., Nakahara, F., Cruz, C.D., Finley, L.W.S., and Frenette, P.S. (2017). Adrenergic nerves activate an angio-metabolic switch in prostate cancer. Science *358*, 321–326.

Zahalka, A.H., and Frenette, P.S. (2020). Nerves in cancer. Nat. Rev. Cancer *20*, 143–157.

Zeng, H., Lu, B., Zamponi, R., Yang, Z., Wetzel, K., Loureiro, J., Mohammadi, S., Beibel, M., Bergling, S., Reece-Hoyes, J., et al. (2018). mTORC1 signaling suppresses Wnt/beta-catenin signaling through DVL-dependent regulation of Wnt receptor FZD level. Proc. Natl. Acad. Sci. U S A *115*, E10362–E10369.

Zhang, P., Yang, M., Zhang, Y., Xiao, S., Lai, X., Tan, A., Du, S., and Li, S. (2019). Dissecting the single-cell transcriptome network underlying gastric premalignant lesions and early gastric cancer. Cell Rep. *27*, 1934–1947 e5.

Zhang, S., Li, Y., Wu, Y., Shi, K., Bing, L., and Hao, J. (2012). Wnt/beta-catenin signaling pathway upregulates c-Myc expression to promote cell proliferation of P19 teratocarcinoma cells. Anat. Rec. (Hoboken) *295*, 2104–2113.

Zhao, C.M., Hayakawa, Y., Kodama, Y., Muthupalani, S., Westphalen, C.B., Andersen, G.T., Flatberg, A., Johannessen, H., Friedman, R.A., Renz, B.W., et al. (2014). Denervation suppresses gastric tumorigenesis. Sci. Transl. Med. *6*, 250ra115.

Zoncu, R., Efeyan, A., and Sabatini, D.M. (2011). mTOR: from growth signal integration to cancer, diabetes and ageing. Nat. Rev. Mol. Cell Biol. *12*, 21–35.

iScience, Volume *24*

Supplemental Information

Neural signaling modulates metabolism of gastric cancer

Hanne-Line Rabben, Gøran Troseth Andersen, Magnus Kringstad Olsen, Anders Øverby, Aleksandr Ianevski, Denis Kainov, Timothy Cragin Wang, Steinar Lundgren, Jon Erik Grønbech, Duan Chen, and Chun-Mei Zhao

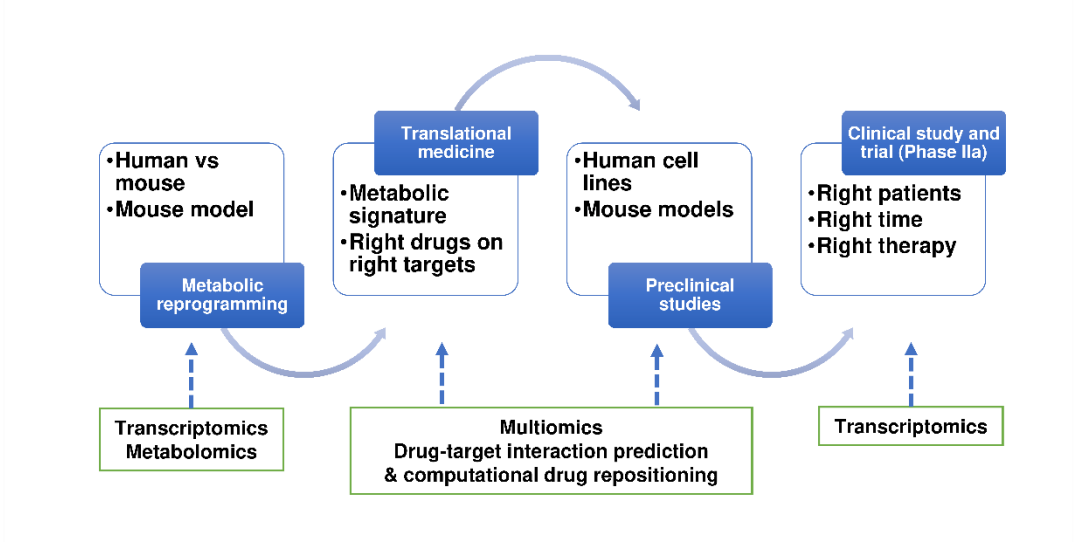

Figure S1, Study design, related to Figure 1: Drawing showing study design of translational research approach and methodology used (indicated in arrows).

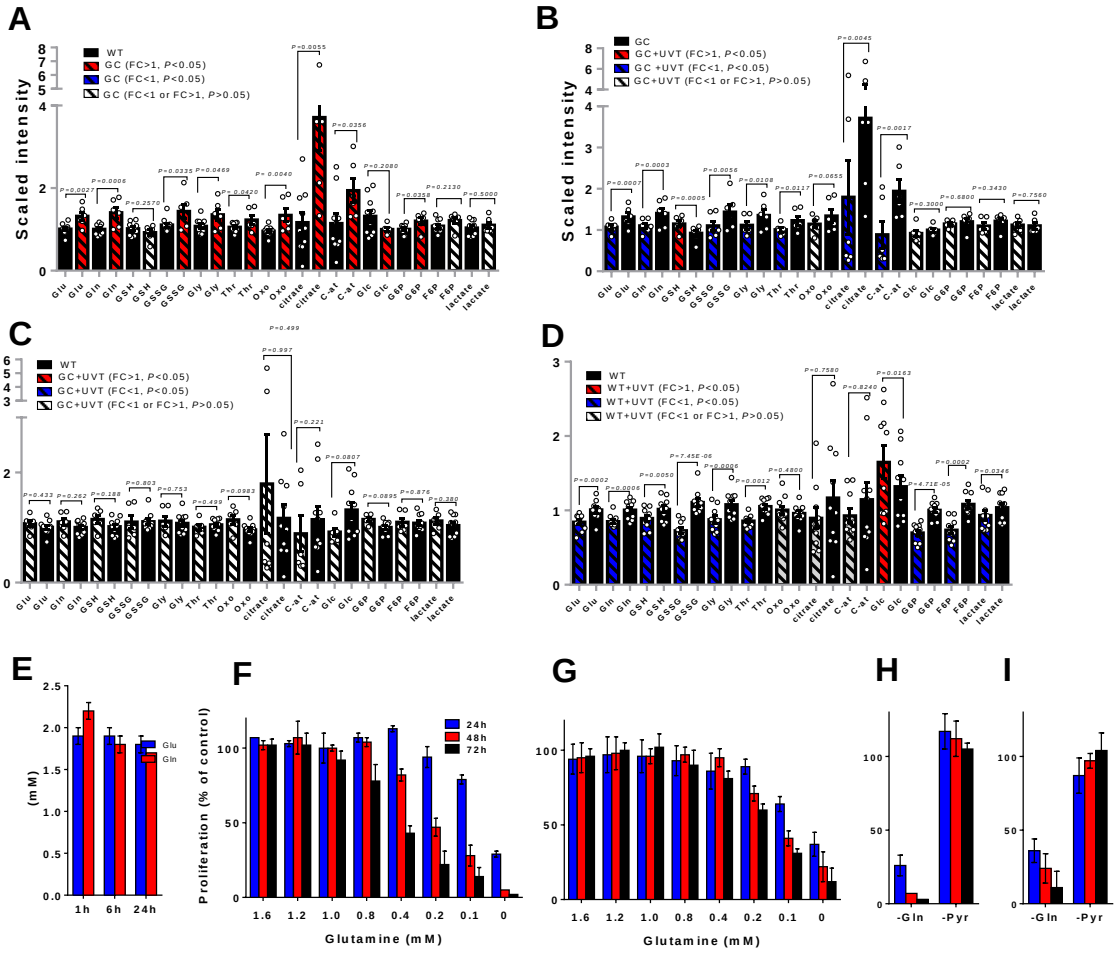

Figure S2, Gastric cancer is glutamine-dependent, related to Figure 4: Levels of metabolites in mouse gastric cancer (GC) (marked in black), wild-type WT (blue), GC after vagotomy (VT) (red) and WT after vagotomy (VT) (purple)(**A-D**) related to **Figure 4.** Glu: L-glutamate; Gln: L-glutamine; GSH: reduced glutathione; GSSG: oxidized glutathione; Gly: glycine; Thr: threonine; Oxo: 5-oxoproline; C-at: cis-aconitate; Glc: glucose; G6P: glucose-6-phosphate; F6P: fructose-6-phosphate. Bars represent relative scaled intensities with SEM and one-way ANOVA p-values. The values were as same as ones in **Figure. 4B-N.** For detailed information, see Table S6. Endogenous levels of L-glutamate and L-glutamine in gastric cancer cells AGS during culture period from 1 to 24 hrs (**E**). Gln reduction (**F,G**) and Gln or Pyr depletion (**H,I**) in the medium in AGS (**F,H**) and MKN45 (**G,I**) cell culture periods of 24, 48 and 72 hrs. Mean of n=3-12 replicates/treatment with SD. Proliferation was assessed using Cell count reagent SF and cell proliferation was calculated relative to controls.

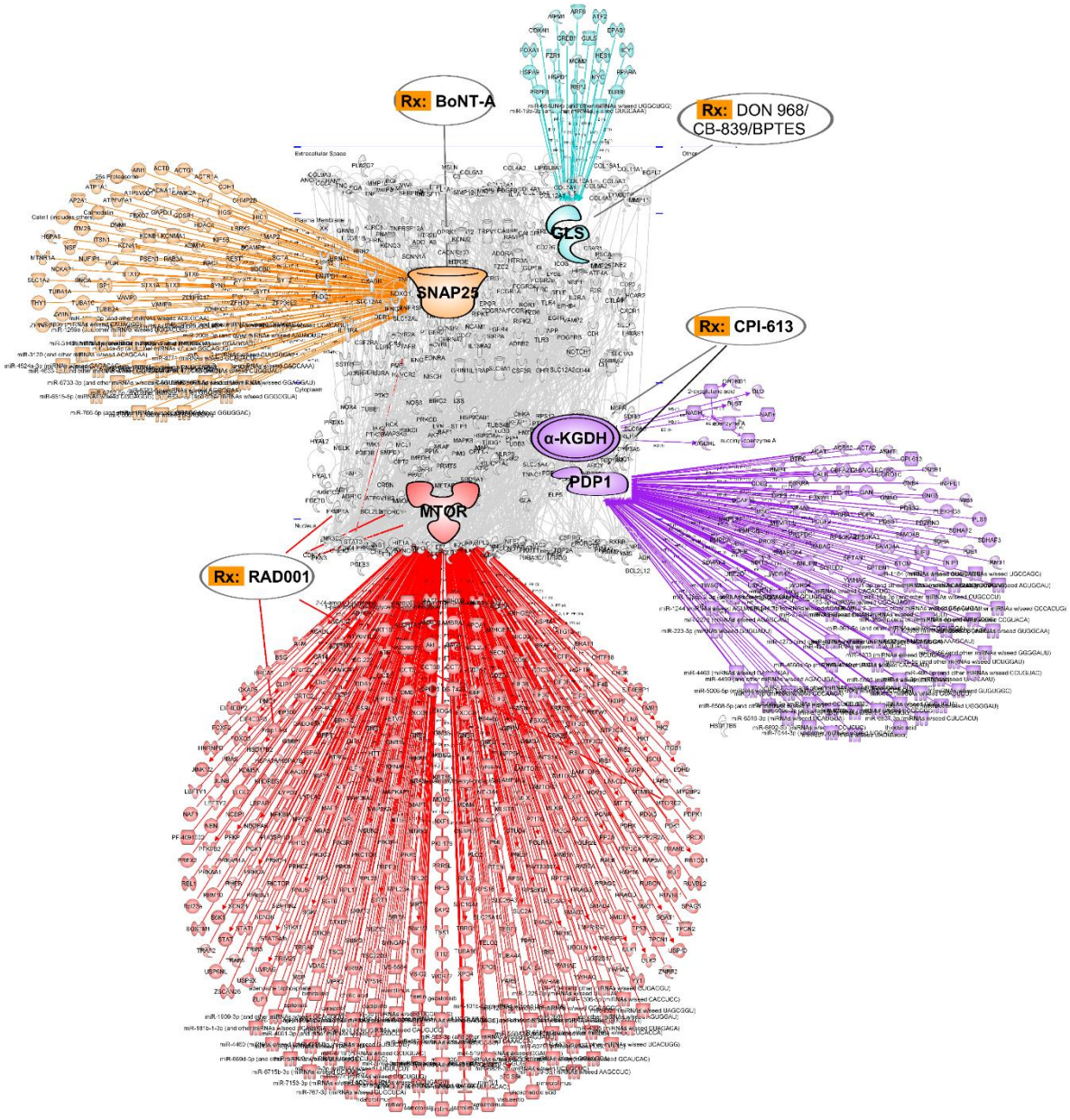

Figure S3, Drug target prediction, related to Figure 6: Waterdrop diagrams showing drug-target interaction prediction and computational drug repositioning in human GC. Note: nodes of RAD001-targeted mTOR (marked in red), CPI-613-targeted PDP1 and α-KGDH (also known as OGDH, purple), BoNT-A-targeted SNAP25 (yellow) and L-DON/968/CB-839/BPTES-targeted GLS (light blue). Lines represent biological interactions between molecules that include proteins, genes, mRNAs, microRNA, lncRNAs and metabolites, generated from differentially expressed drug target genes (only drug targets differentially expressed at $p<0.05$, $q<0.05$ are shown).

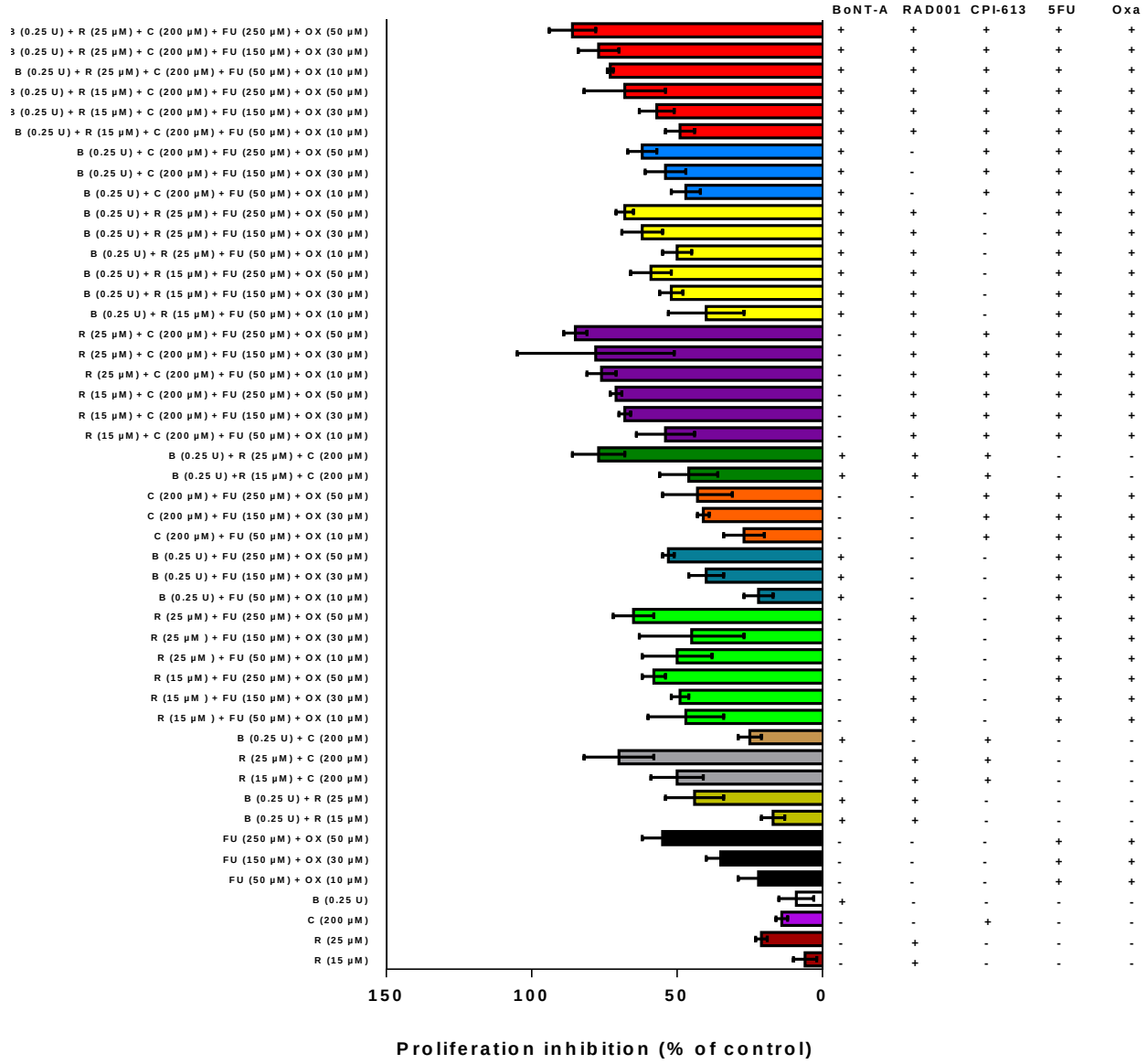

Figure S4, *In vitro* drug screening, related to Figure 7: Proliferation inhibition rates of *in vitro* treatment of BoNT-A, RAD001, CPI-613, 5-FU and oxaliplatin either alone or in different combinations at increasing doses using MKN74 cells. Mean of n=3-12 replicates/treatment with SD. Proliferation was measured using CCK-8 Kit at 450 nm and treatments were normalized to respective vehicle controls.

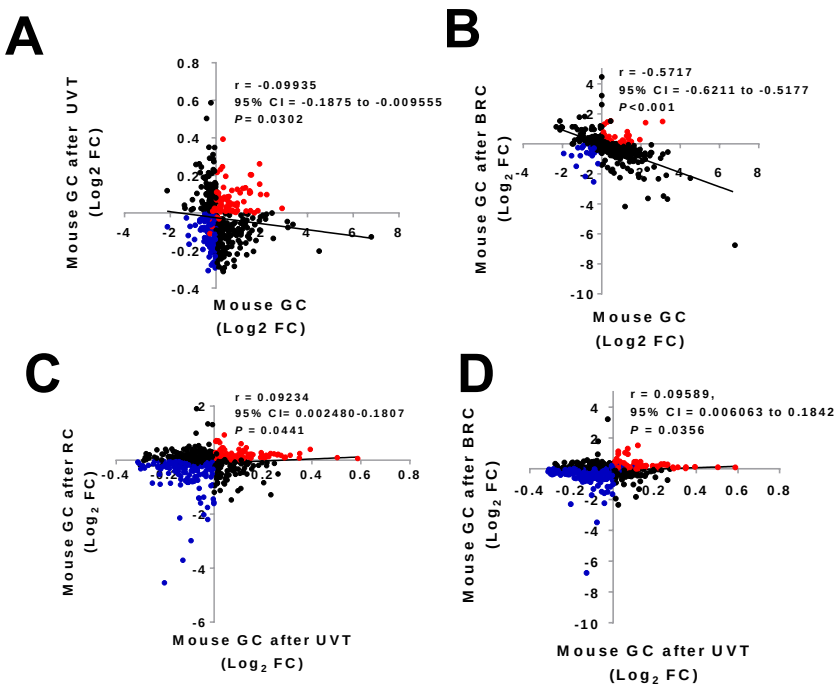

Figure S5, Nerve-cancer metabolism in gastric cancer, related to Figure 8A: Transcriptome profiling of genes involved in the nerve-cancer metabolism pathways of synaptogenesis signaling pathway, WNT/β-catenin signaling, mTOR pathway and energy metabolism. Correlations between mouse GC with *vs.* without unilateral vagotomy (UVT)(**A**), between mouse GC with *vs.* without BRC (**B**), between mouse GC with RC *vs.* UVT (**C**), and between mouse GC with BRC *vs.* UVT (**D**). Linear regression lines were drawn using GraphPad Prism v6. Pearson's test for correlation was used.

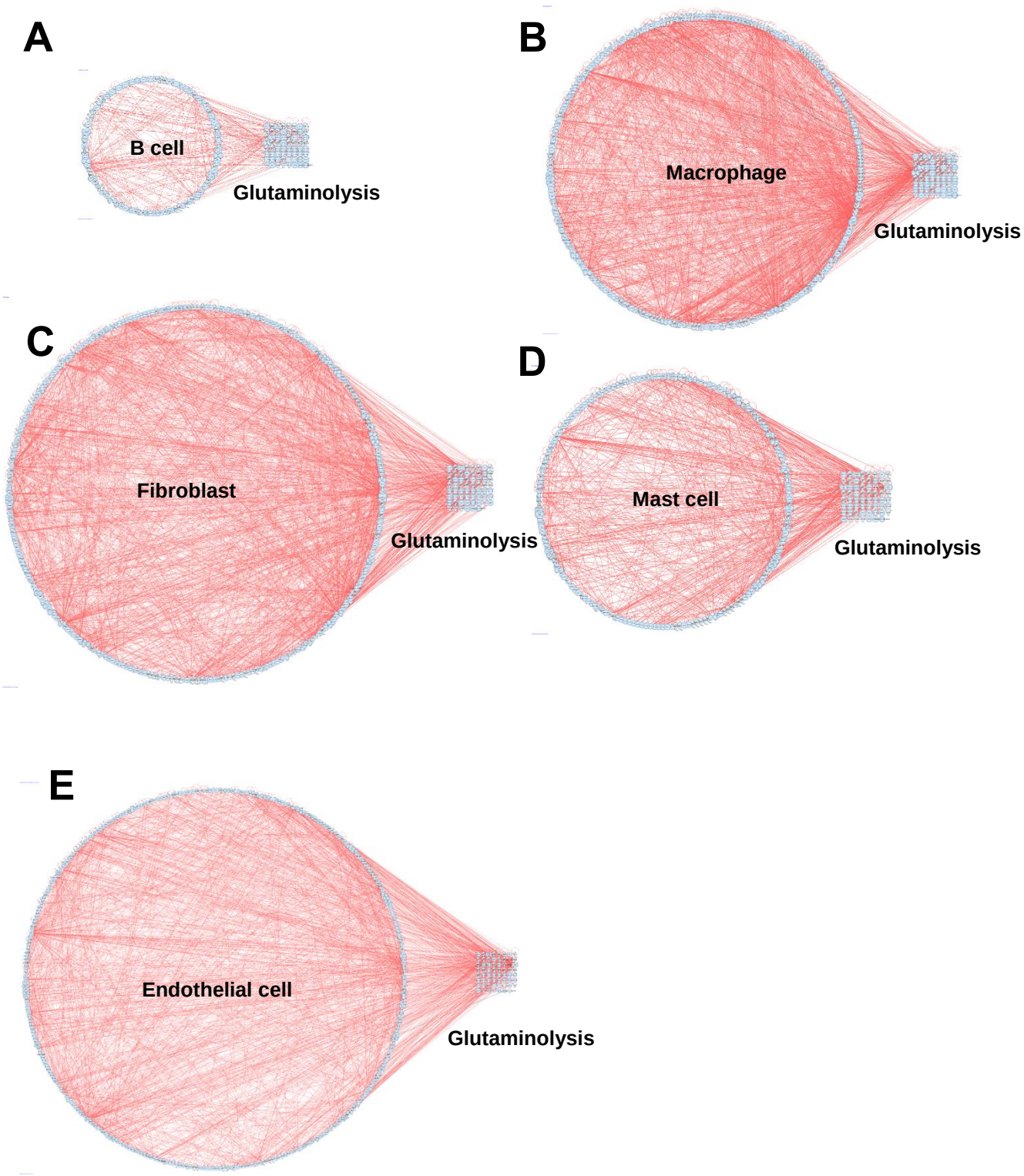

Figure S6, Single-cell atlas and glutamine pathways, related to Figure 8C-D: Computational network modeling showing interactions within B cell gene markers (**A**), macrophage gene markers (**B**), fibroblast gene markers (**C**), mast cell gene markers (**D**) and endothelial cell gene markers (**E**) and connections between the cell types and glutaminolysis (**A-E**) based the single-cell transcriptome atlas (Zhang et al., 2019)(GSE134520).

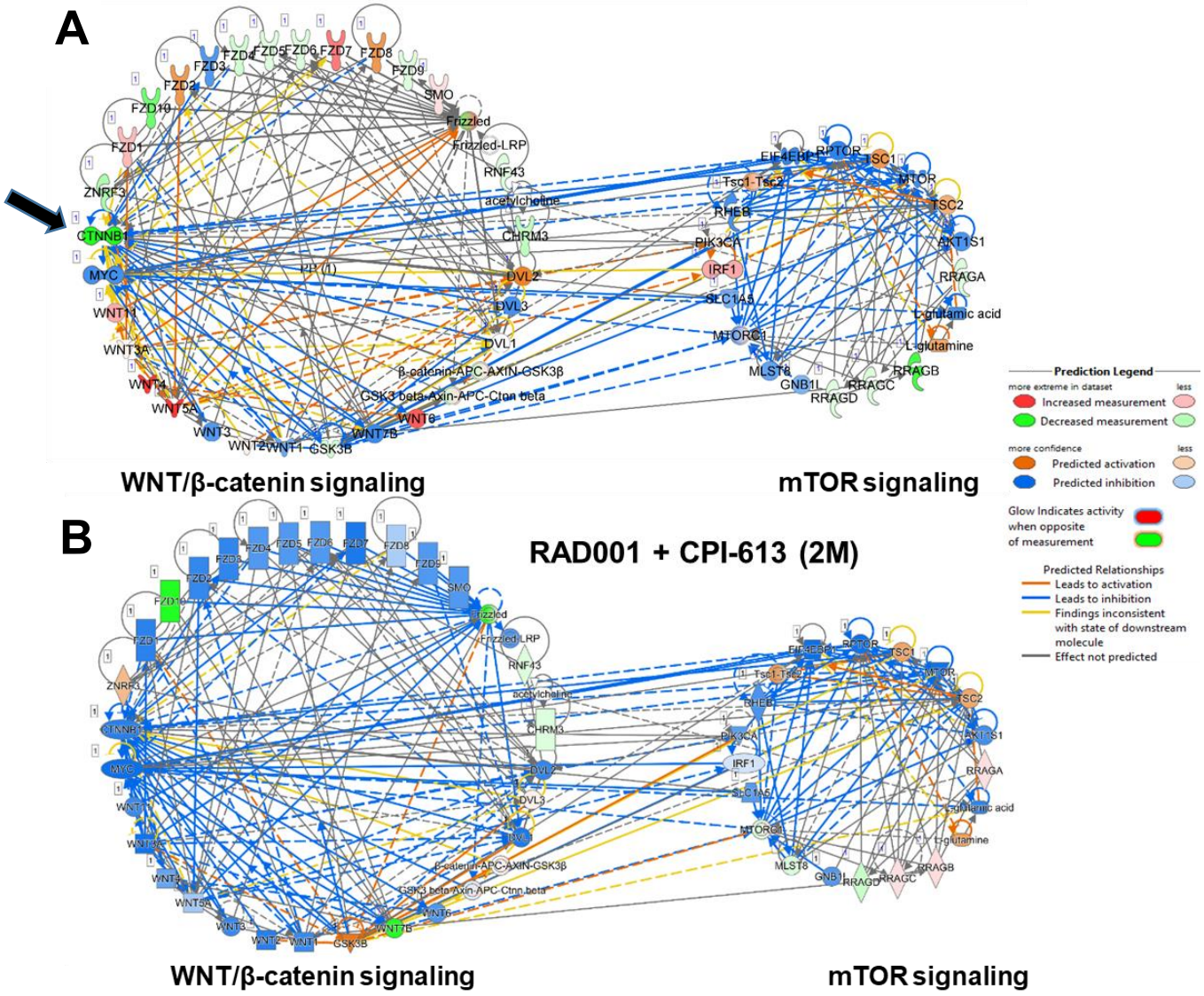

Figure S7, *In silico* modelling, related to Figure 8: Representative prediction of downstream effect of *in silico* inhibition of the CTNNB1 node (marked in green and annotated by black arrow) in the WNT signaling cluster (left) on mTOR signaling (right)(**A**) and effects of treatment of RC for 2 months (2M) on WNT/β-catenin signaling pathway and mTOR signaling clusters (**B**). Overlay gene expression: GC *vs.* WT. MAP (molecular activity prediction) to generate predictions. Semi-quantitative method: dark blue represent -2, light blue represent -1, white represent 0, light orange represent +1 and dark orange represent +2.

Table S1, Genes detected by real-time PCR and RNAseq, related to Figure 1: List of genes detected by both RNAseq and real-time PCR and correlation analysis (figure).

	GenBank	Gene		GenBank	Gene
1	**NM_010347**	Aes	54	**NM_133955**	Rhou
2	**NM_007462**	Apc	55	**NM_029457**	Senp2
3	**NM_009733**	Axin1	56	**NM_013834**	Sfrp1
4	**NM_029933**	Bcl9	57	**NM_009144**	Sfrp2
5	**NM_009771**	Btrc	58	**NM_016687**	Sfrp4
6	**NM_023465**	Ctnnbip1	59	**NM_012030**	Slc9a3r1
7	**NM_007631**	Ccnd1	60	**NM_011441**	Sox17
8	**NM_009829**	Ccnd2	61	**NM_009309**	T
9	**NM_007632**	Ccnd3	62	**NM_009332**	Tcf3
10	**NM_146087**	Csnk1a1	63	**NM_009331**	Tcf7
11	**NM_139059**	Csnk1d	64	**NM_011599**	Tle1
12	**NM_007788**	Csnk2a1	65	**NM_019725**	Tle2
13	**NM_013502**	Ctbp1	66	**NM_011915**	Wif1
14	**NM_009980**	Ctbp2	67	**NM_018865**	Wisp1
15	**NM_007614**	Ctnnb1	68	**NM_021279**	Wnt1
16	**NM_172464**	Daam1	69	**NM_009518**	Wnt10a
17	**NM_178118**	Dixdc1	70	**NM_009519**	Wnt11
18	**NM_010051**	Dkk1	71	**NM_053116**	Wnt16
19	**NM_010091**	Dvl1	72	**NM_023653**	Wnt2
20	**NM_007888**	Dvl2	73	**NM_009520**	Wnt2b
21	**NM_177821**	Ep300	74	**NM_009521**	Wnt3
22	**NM_134015**	Fbxw11	75	**NM_009522**	Wnt3a
23	**NM_013890**	Fbxw2	76	**NM_009523**	Wnt4
24	**NM_013907**	Fbxw4	77	**NM_009524**	Wnt5a
25	**NM_010202**	Fgf4	78	**NM_009525**	Wnt5b
26	**NM_010235**	Fosl1	79	**NM_009526**	Wnt6
27	**NM_008238**	Foxn1	80	**NM_009527**	Wnt7a
28	**NM_008043**	Frat1	81	**NM_009528**	Wnt7b
29	**NM_011356**	Frzb	82	**NM_009290**	Wnt8a
30	**NM_008045**	Fshb	83	**NM_011720**	Wnt8b
31	**NM_021457**	Fzd1	84	**NM_139298**	Wnt9a
32	**NM_020510**	Fzd2	85	**NM_010368**	Gusb
33	**NM_021458**	Fzd3	86	**NM_013556**	Hprt1
34	**NM_008055**	Fzd4	87	**NM_008302**	Hsp90ab1
35	**NM_022721**	Fzd5	88	**NM_008084**	Gapdh
36	**NM_008056**	Fzd6	89	**NM_007393**	Actb
37	**NM_008057**	Fzd7	90	**SA_00106**	MGDC
38	**NM_008058**	Fzd8	91	**SA_00104**	RTC
39	**NM_019827**	Gsk3b	92	**SA_00104**	RTC
40	**NM_010591**	Jun	93	**SA_00104**	RTC
41	**NM_032396**	Kremen1	94	**SA_00103**	PPC
42	**NM_010703**	Lef1	95	**SA_00103**	PPC
43	**NM_008513**	Lrp5	96	**SA_00103**	PPC
44	**NM_008514**	Lrp6			
45	**NM_010849**	Myc			
46	**NM_027280**	Nkd1			
47	**NM_008702**	Nlk			
48	**NM_011098**	Pitx2			
49	**NM_023638**	Porcn			
50	**NM_019411**	Ppp2ca			
51	**NM_016891**	Ppp2r1a			
52	**NM_009358**	Ppp2r5d			
53	**XM_134865**	Pygo1			

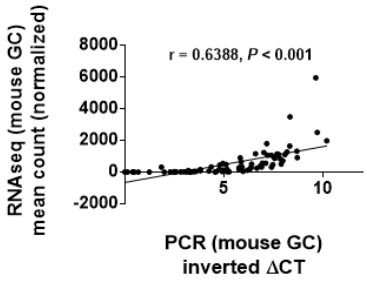

Table S2, Upstream regulators in mouse GC, related to Figure 2F: Upstream analysis of WNT/β-catenin pathway regulators and mTOR targets in mouse GC, related to **Figure 2F.** Predicted Activation State was Activated for z-score>2.000.

Upstream Regulator	Log_2 FC	Predicted Activation State	Activation z-score	p-value of overlap	Target Molecules in Dataset	Target molecules in mTOR pathway	Molecules
Tgf beta		Activated	3.848	2.99E-07	65	0	
WNT1	0.000	Activated	3.138	6.85E-03	34	3	EIF3C,MRAS,PDPK1
CD44	1.156	Activated	3.695	6.05E-08	55	0	
JUN	0.184	Activated	2.219	5.21E-03	55	1	RHOB
TGFB1	0.727	Activated	5.957	2.39E-17	236	3	PPP2CA,PRKCG,RHOA
TGFBR1	-0.536	Activated	2.735	5.98E-04	20	0	
TGFB2	1.573	Activated	3.309	4.55E-11	34	0	
CTNNB1	0.208	Activated	3.741	4.53E-10	165	1	PPP2CA

Table S3, Metabolite signature, related to Figure 4: List of metabolites of gastric cancer (GC) mice and wild-type (WT) mice presented in **Figure 4A.** *GC: gastric cancer; WT: wild-type; FC: Fold change.* Green: p≤0.05, fold change <1.00; Red: p≤ 0.05, fold change ≥1.0. White: p<0.05, 1.0 ≤ fold change >1.0.

Metabolite	Mouse GC *vs.* WT (FC)	Mouse GC after vagotomy *vs.* GC (FC)	Mouse GC after vagotomy *vs.* WT (FC)	Mouse WT after vagotomy *vs.* WT (FC)
prostaglandin B2	4.92	0.54	2.63	0.94
1-arachidonoyl-2-hydroxy-sn-glycero-3-phosphoethanolamine	2.64	0.52	1.36	0.64
inositol 1-phosphate	1.46	0.78	1.14	0.80
docosahexaenoic acid	0.75	1.32	1.00	1.16
gamma-butyrobetaine	0.74	1.22	0.90	1.14
8Z,11Z,14Z-eicosatrienoic acid	0.74	1.45	1.08	0.87
adrenic acid	0.71	1.34	0.95	0.90
13,16-docosadienoic acid	0.65	1.35	0.87	1.06
phosphorylcholine	0.64	1.17	0.75	0.95
propionyl-L-carnitine	0.63	1.71	1.07	1.35
sn-glycero-3-phosphocholine	0.60	1.48	0.89	1.02
arachidonic acid	0.59	1.51	0.88	0.97
icosapent	0.54	1.84	0.99	0.95
1-stearoyl-2-hydroxy-sn-glycero-3-phosphoethanolamine	0.53	1.48	0.79	0.85
cis-4,7,10,13,16-docosapentaenoic acid	0.52	1.64	0.85	1.02
eicosa-11Z, 14Z-dienoic acid	0.51	1.59	0.82	1.01
rac-1-stearoylglycerol	0.47	1.83	0.87	1.09
sn-glycerol-3-phosphate	0.46	1.49	0.69	1.08
3-dehydrocarnitine	0.45	1.11	0.50	0.96
1-palmitoyl-2-hydroxy-sn-glycero-3-phosphoethanolamine	0.44	1.79	0.78	0.91
1-oleoyl-lysophosphatidylethanolamine	0.39	1.82	0.71	0.84
D-sphingosine	0.35	1.87	0.66	0.90
oleoylcarnitine	0.32	2.19	0.71	1.22
citric acid	3.18	0.48	1.54	0.77
cis-aconitic acid	1.70	0.46	0.78	0.81
N-acetyl-L-methionine	2.08	0.59	1.22	0.63
S-glutathionyl-L-cysteine	1.56	0.64	1.00	0.79
L-glutamine	1.40	0.78	1.10	0.85
L-glutamic acid	1.31	0.81	1.06	0.84
glutathione disulfide	1.30	0.77	0.99	0.66
glycine	1.26	0.83	1.04	0.81
L-threonine	1.17	0.82	0.96	0.82
betaine	0.75	1.14	0.86	1.15
5-hydroxytryptamine	0.63	1.36	0.86	1.08
histamine	0.59	1.38	0.81	1.02
gamma-glutamylglutamate	2.15	0.55	1.18	0.83
glycylleucine	1.51	0.82	1.24	0.94
gamma-glutamyl-leucine	1.38	0.76	1.05	1.00
inosine	0.72	1.44	1.03	1.14

deoxyinosine	**0.56**	**1.80**	1.00	**1.63**
guanosine	**0.52**	**1.81**	0.93	**1.55**
deoxyguanosine	**0.46**	**2.36**	1.08	**1.70**
4'-phosphopantetheine	**0.69**	**1.24**	0.86	**0.84**
5-methyltetrahydrofolic acid	**0.68**	**1.73**	1.18	**1.45**
coenzyme A	**0.55**	**1.54**	0.85	0.84
dephospho-coenzyme A	**0.54**	**2.30**	1.25	1.16
beta-glycerophosphoric acid	**0.56**	**1.58**	0.88	1.18
hippuric acid	**0.21**	**1.41**	0.30	**1.25**

Table S4, Energy metabolites, related to Figure 4B-N: Statistic data corresponding to metabolites shown in **Figure 4B-N and Figure S2A-D.**

	WT	***WT (+UVT)***	***GC***	***GC (+UVT)***	***WT v GC***	***GC (+UVT) v GC***	***GC (+)UVT v WT***	***WT (+UVT) v WT***
	Mean ± SEM	**Mean** ± SEM	**Mean** ± SEM	**Mean** ± SEM	***p*-value**	***p*-value**	***p*-value**	***p*-value**
Glu	**1.0058** ±0.041	**0.8414** ±0.0345	**1.3163** ±0.0995	**1.0686** ±0.0582	2.70E-03	7.00E-04	4.33E-01	2.00E-04
Gln	**1.0034**±0.0389	**0.8494** ±0.0263	**1.4036** ±0.1324	**1.1014** ±0.0692	6.00E-04	3.00E-04	2.62E-01	6.00E-04
GSH	**1.0143**±0.0482	**0.8903** ±0.0427	**0.9225** ±0.0757	**1.1482** ±0.0755	2.57E-01	5.00E-04	1.88E-01	5.00E-03
GSSG	**1.1073**±0.0499	**0.7275** ±0.0381	**1.436** ±0.1722	**1.0995** ±0.1168	3.35E-02	5.60E-03	8.03E-01	7.45E-06
Gly	**1.0762**±0.0582	**0.8745** ±0.0509	**1.3519** ±0.1394	**1.1159** ±0.0929	4.69E-02	1.08E-02	7.53E-01	6.00E-04
Thr	**1.0502**±0.0332	**0.8572** ±0.0248	**1.2261** ±0.1052	**1.0057** ±0.0528	4.20E-02	1.17E-02	4.99E-01	1.20E-03
Oxo	**0.9594**±0.0373	**1.0037** ±0.0543	**1.3394** ±0.1572	**1.1404** ±0.0842	4.00E-03	6.55E-02	9.83E-02	0.48E-01
citrate	**1.1665**±0.2424	**0.8943** ±0.1402	**3.7086** ±0.787	**1.7935** ±0.8935	5.50E-03	4.50E-03	9.97E-01	7.58E-01
C-at	**1.1432**±0.2318	**0.9253** ±0.0949	**1.9406** ±0.2825	**0.8868** ±0.3289	3.56E-02	1.70E-03	2.21E-01	8.24E-01
Glc	**1.3181**±0.1462	**1.6463** ±0.2223	**0.9975** ±0.0467	**0.9161** ±0.0768	2.08E-01	3.00E-01	8.07E-02	1.63E-02
G6P	**1.0018**±0.0352	**0.6972** ±0.039	**1.2008** ±0.084	**1.1456** ±0.0344	3.58E-02	6.80E-01	8.95E-02	4.71E-05
F6P	**1.0808**±0.0486	**0.7342** ±0.0466	**1.213** ±0.0772	**1.0979** ±0.0733	2.13E-01	3.43E-01	8.76E-01	2.00E-04
lactate	**1.0359**±0.058	**0.9311** ±0.0669	**1.1007** ±0.0744	**1.1203** ±0.0641	5.00E-01	7.56E-01	3.80E-01	3.46E-02

Mean: scaled intensity of N=10 (WT) or N=6 (GC), *p*-value: One-way ANOVA test between groups, GC: Gastric cancer, WT: wild-type, UVT: Unilateral vagotomy, Glu: L-glutamate, Gln: L-glutamine, GSH: glutathione, reduced, GSSG: glutathione, oxidized, Gly: glycine, Thr: threonine, Oxo: 5-oxoproline, C-at: cis-aconitate, Glc: glucose, G6P: fructose-6-phosphate, F6P: fructose-6-phosphate.

Table S5, Signaling pathways involved in mouse gastric cancer (GC), related to Figure 5A: Multi-omics integrative analysis in IPA revealed 41 signaling pathways that appeared exclusively in Mouse GC *vs*. WT.

Common signaling pathway (IPA)	**Transcriptomics**		**Metabolomics**	
	-log$_{10}$(*P*)	**Z-score**	**-log$_{10}$(*P*)**	**Z-score**
Ethanol Degradation II	1.49E00	-0.632	3.46E-01	N/A
Acyl Carrier Protein Metabolism	7.12E-01	N/A	2.17E00	N/A
β-alanine Degradation I	4.55E-01	N/A	2.29E00	N/A
Glycine Degradation (Creatine Biosynthesis)	4.55E-01	N/A	1.38E00	N/A
Granulocyte Adhesion and Diapedesis	5.38E00	N/A	1.31E00	N/A
Leucine Degradation I	2.00E00	-1.890	7.03E-01	N/A
Synaptogenesis Signaling Pathway	1.79E00	2.887	4.83E-01	N/A
L-cysteine Degradation III	3.21E-01	N/A	1.38E00	N/A
Sphingosine-1-phosphate Signaling	2.20E00	-0.343	7.42E-01	N/A
Role of MAPK Signaling in the Pathogenesis of Influenza	1.35E00	N/A	8.57E-01	N/A
Glutamate Receptor Signaling	2.68E-01	2.000	2.47E00	N/A
Colorectal Cancer Metastasis Signaling	2.71E00	2.689	6.58E-01	N/A
Oleate Biosynthesis II (Animals)	2.00E00	-0.816	1.51E00	N/A
Aspartate Degradation II	3.89E-01	N/A	1.38E00	N/A
UDP-N-acetyl-D-glucosamine Biosynthesis II	1.04E00	N/A	1.86E00	N/A
Isoleucine Degradation I	2.00E00	-1.890	1.48E00	N/A
Glutamate Degradation II	3.21E-01	N/A	1.51E00	N/A
Valine Degradation I	3.92E00	-2.714	1.34E00	N/A
FXR/RXR Activation	9.43E-01	N/A	1.86E00	N/A
Endocannabinoid Neuronal Synapse Pathway	7.12E-01	1.890	1.57E00	N/A
Taurine Biosynthesis	4.55E-01	N/A	1.51E00	N/A

Fatty Acid β-oxidation I	2.37E-01	N/A	3.21E-01	N/A
Serotonin Degradation	1.78E00	-1.886	1.34E00	N/A
Acetyl-CoA Biosynthesis I (Pyruvate Dehydrogenase Complex)	1.82E00	-2.000	6.58E-01	N/A
Neuroinflammation Signaling Pathway	2.49E00	3.250	7.88E-01	N/A
Prostanoid Biosynthesis	1.76E00	0.447	1.51E00	N/A
Human Embryonic Stem Cell Pluripotency	3.32E00	N/A	6.58E-01	N/A
Trna Splicing	2.22E00	0.775	5.30E-01	N/A
Adenine and Adenosine Salvage III	4.80E-01	N/A	1.99E00	N/A
Purine Ribonucleosides Degradation to Ribose-1-phosphate	4.80E-01	N/A	2.72E00	N/A
Glutathione Biosynthesis	3.21E-01	N/A	2.29E00	N/A
Ethanol Degradation IV	2.14E00	0.000	3.75E-01	N/A
Fcγ Receptor-mediated Phagocytosis in Macrophages and Monocytes	2.41E00	1.890	5.88E-01	N/A
Phospholipase C Signaling	3.39E00	0.832	4.83E-01	N/A
Eicosanoid Signaling	2.02E00	0.905	1.27E00	N/A
Branched-chain α-keto acid Dehydrogenase Complex	1.60E00	N/A	6.58E-01	N/A
Purine Nucleotides Degradation II (Aerobic)	3.23E-01	2.000	1.34E00	N/A
Endothelin-1 Signaling	2.14E00	1.820	2.78E-01	N/A
L-cysteine Degradation I	7.64E-01	N/A	1.38E00	N/A
2-oxobutanoate Degradation I	2.22E00	-2.000	3.46E-01	N/A
Flavin Biosynthesis IV (Mammalian)	4.55E-01	N/A	1.51E00	N/A

Table S6, Signaling pathways involved in mouse gastric cancer (GC) after vagotomy, related to Figure 5B: Multi-omics integrative analysis in IPA revealed 24 signaling pathways that appeared exclusively in mouse GC after vagotomy *vs.* sham operation.

Common signaling pathway (IPA)	**Transcriptomics**		**Metabolomics**	
	-log$_{10}$(*P*)	**Z-score**	**-log$_{10}$(*P*)**	**Z-score**
Vitamin-C Transport	2.60E-01	N/A	1.88E00	N/A
Phosphatidylcholine Biosynthesis I	7.01E-01	N/A	1.57E00	N/A
CDP-diacylglycerol Biosynthesis I	2.17E+00	-0.707	1.49E00	N/A
Synaptic Long Term Depression	4.92E-01	-1.706	1.66E00	N/A
Coenzyme A Biosynthesis	4.99E-01	N/A	2.61E00	N/A
Superpathway of Serine and Glycine Biosynthesis I	1.39E00	N/A	1.42E00	N/A
Gαq Signaling	1.89E+00	-1.961	7.14E-01	N/A
Amyotrophic Lateral Sclerosis Signaling	2.25E00	-0.626	1.66E00	N/A
Tetrapyrrole Biosynthesis II	9.55E-01	N/A	1.76E00	N/A
tRNA Charging	7.93E-01	-1.134	1.61E00	2.000
Pyrimidine Ribonucleotides Interconversion	4.13E-01	-2.449	1.49E00	N/A
Purine Nucleotides De Novo Biosynthesis II	2.22E00	0.447	1.37E00	N/A
Phosphatidylglycerol Biosynthesis II (Non-plastidic)	1.95E00	-0.707	1.24E00	N/A
Serine Biosynthesis	1.85E00	N/A	6.7E-01	N/A
5-aminoimidazole Ribonucleotide Biosynthesis I	1.41E00	N/A	2.2E00	N/A
Glutathione Redox Reactions I	3.64E-01	N/A	1.88E00	N/A
Adipogenesis pathway	4.18E-01	N/A	1.58E00	N/A
Stearate Biosynthesis I (Animals)	1.50E00	-1.897	5.04E-01	N/A
Arsenate Detoxification I (Glutaredoxin)	3.99E-01	N/A	1.42E00	N/A
Serotonin and Melatonin Biosynthesis	3.28E-01	N/A	1.49E00	N/A
Triacylglycerol Biosynthesis	1.14E00	-1.000	1.42E00	N/A
Antioxidant Action of Vitamin C	0.00E00	2.530	2.02E00	N/A
Ascorbate Recycling (Cytosolic)	4.99E-01	N/A	1.76E00	N/A

Ceramide Signaling	1.62E00	-1.414	9.96E-01	N/A

Table S7, Signaling pathways involved in mouse gastric cancer (GC) with and without vagotomy, related to Figure 5C: Multi-omics integrative analysis in IPA revealed 13 signaling pathways present in comparison between mouse GC *vs.* WT and in mouse GC after vagotomy *vs.* sham operation.

Common signaling pathway (IPA)	**Mouse GC *vs.* WT**				**Mouse GC after vagotomy**			
	Transcripts		**Metabolites**		**Transcripts**		**Metabolites**	
	-log$_{10}$(*P*)	**Z-score**	**-log$_{10}$(*P*)**	**Z-score**	**-log$_{10}$(*P*)**	**Z-score**	**-log$_{10}$(*P*)**	**Z-score**
Gap Junction Signaling	2.6E00	N/A	8.93E-01	N/A	6.31E-01	N/A	1.36E00	N/A
Phospholipases	1.71E00	1.886	4.06E-01	N/A	0.00E00	-2.449	1.57E00	N/A
Sirtuin Signaling Pathway	3.17E-01	0.949	1.71E00	N/A	2.34E00	-1.029	6.68E-01	N/A
Protein Kinase A Signaling	1.61E00	-0.232	3.46E-01	N/A	2.45E00	-1.089	5.61E-01	N/A
Asparagine Biosynthesis I	7.12E-01	N/A	1.38E00	N/A	9.24E-01	N/A	1.88E00	N/A
TCA Cycle II (Eukaryotic)	5.51E-01	-2.449	2.91E00	N/A	2.77E-01	N/A	1.97E00	N/A
Choline Biosynthesis III	2.71E00	0.378	4.41E-01	N/A	2.03E00	-1.342	1.66E00	N/A
γ-glutamyl Cycle	3.33E00	0.707	2.58E00	N/A	3.68E-01	N/A	2.39E00	N/A
Leukotriene Biosynthesis	1.77E00	2.449	1.02E00	N/A	1.34E00	-1.000	2.61E00	N/A
Agranulocyte Adhesion and Diapedesis	5.38E00	N/A	1.31E00	N/A	4.78E-01	N/A	1.58E00	N/A
Superpathway of Methionine Degradation	9.67E-01	-2.530	2.31E00	2.236	0.00E00	1.000	1.96E00	-2.000
Calcium Signaling	1.52E00	1.826	1.27E00	N/A	7.62E-01	-2.236	1.76E00	N/A
Glutathione-mediated Detoxification	1.02E00	-0.707	1.75E00	N/A	1.16E00	-1.633	3.75E00	-1.000

Table S8, Baseline patient data, related to Figure 8L: Baseline patient data (the first patient was recruited at September 10,

Patient number	Age at inclusion	TNM stage at time of diagnosis	Chemotherapy	TNM stage at inclusion time	Tumor location and size
1	81	T4N1M1	1st line treatment, stopped due toxic side effects	T4N1M1	Greater curvature, lesser curvature and anterior wall. Longest diameter 9 cm
2	70	T3N0M0	Neoadjuvant chemotherapy, inoperabel due to comorbidity	T3N1M0	Cardia and proximal esophagus. Longest diameter 3 cm
3	79	T4aN2M1	Palliativ chemotherapy with EOX	T4aN2M1	Distal part of the stomach. Circular tumor with longest diameter 8 cm
4	49	TxNxM1	1st line treatment, 2nd line treatment.	TxNxM1	Cardia. Extensive liver metastasis
5	83	TxNxMx	No previous chemotherapy due to age and comorbidity	T4aN3M1	Cardia. Extensive liver metastasis
6	84	T4aN3M0	No previous chemotherapy due to age and comorbidity	T4aN3M0	Linitis plastica in whole stomach except the most proximal part

2014).

Note: One additional patient (i.e. patient no. 7) gave his consent for participation in this study, but pretreatment CT scan of the stomach showed no measurable tumor size. According to the study protocol (Supplementary Data Clinical study protocol), this patient was excluded from further participation in the study and did not receive BoNT-A treatment.

Table S9, Primary outcome measures, related to Figure 8L: Primary outcome measure: Tumor evaluation

Patient number	Tumor thickness, diameter or volume density (mean±SD % before BoNT-A injection	Tumor thickness, diameter or volume density (%) 8 weeks after injection	Tumor diameter and volume density (%) 20 weeks after injection
1	14 mm tumor thickness	Not followed (died before the time point)	Not followed (died before the time point)
2	27 x 16 mm, 20x17 mm, 40.8±10.9 %	32x21 mm and 26x20 mm, 34.4±5.3 %	31x21 mm, 28x21 mm, 27.9±10.8 %
3	17-19 mm tumor thickness	Not followed (died before the time point)	Not followed (died before the time point)
4	20x29 mm	Not followed (died before the time point)	Not followed (died before the time point)
5	12 mm tumor thickness	Not followed (died before the time point)	Not followed (died before the time point)

6	22 mm tumor thickness	26 mm tumor thickness	Not followed ((died before the time point)

Table S10, Secondary outcome measure (short term), related to Figure 8L: Secondary outcome measure: Short-time adverse effects and ECOG status after BoNT-A injections

Patient number	Baseline ECOG	Adverse effects during procedure	Adverse effects after observation 24 hours after procedure	Adverse effects at 2 weeks outpatient clinical control	ECOG after 2 weeks
1	1	No	No	No	1
2	2	No	No	No	2
3	1	No	No	No	2
4	1	No	No	No	3
5	1	No	No	No	ECOG status missing from local hospital
6	2	No	No	No	1

Table S11, Secondary outcome measures (long-term), related to Figure 8L. Secondary outcome measure: Long term adverse effects and ECOG status after BoNT-A injections

Patient number	Survival days after BoNT-A injection	8 weeks (56 days) outpatient control performed	Adverse effects /ECOG status	20 weeks control performed	Adverse effects /ECOG status	Any adverse events during the course of the disease until death
1	51	Died before control				Death related to natural progression of disease and no adverse effects recorded until time of death.
2	188	Yes	No/3	Yes	No/3	Death related to natural progression of disease and no adverse effects recorded until time of death.
3	69	Withdrawal from study protocol due to severe progression of disease				Death related to natural progression of disease and no adverse effects recorded until time of death.
4	37	Died before control				Death related to natural progression of disease and no adverse effects recorded until time of death.
5	27	Died before control				Death related to natural progression of disease and no adverse effects recorded until time of death.
6	112	Yes	No/1	No		Death related to natural progression of disease and no adverse effects recorded until time of death.

Table S12, Study groups, related to Figure 7K and Figure 8G-L.

Group	Subjects	Treatment (*N*)(female/male)	Age at intervention	Age at examination
Clinical examination	GC patients	Gastrectomy (16)(6/10)	54-87 years	5 years follow-up
Transcriptomics	**GC mice#**	**UVT (6) (4/2)**	6 months	12 months
Metabolomics	**GC mice**	**UVT (6) (2/4)**	6 months	12 months
		Sham (6)(2/4)	6 months	12 months
	WT mice	**UVT (10)(4/6)**	6 months	12 months
		Sham (10)(4/6)	6 months	12 months
Treatments:	**GC mice**	**UVT + saline (9)(7/2)**	12-14 months	14-16 months
		Sham + saline (9)(7/2)	12-14 months	14-16 months
		UVT + FUOX (16)(10/6)	12-14 months	14-16 months
		Sham + FUOX (16)(10/6)	12-14 months	14-16 months
		Sham + FUOX (16)(10/6)	12-14 months	14-16 months
		Sham + FUOX (16)(10/6)	12-14 months	14-16 months
		BoNT-A + saline (22)(12/10)	12-14 months	14-16 months
		Saline (22)(12/10)	12-14 months	14-16 months
		BoNT-A + FU (12)(7/5)	12-14 months	14-16 months
		FU (12)(7/5)	12-14 months	14-16 months
		BoNT-A + OX (26)(14/12)	12-14 months	14-16 months
		OX (26)(14/12)	12-14 months	14-16 months
		BoNT-A + FUOX (26)(15/11)	12-14 months	14-16 months
		FUOX (26)(15/11)	12-14 months	14-16 months
		BoNT-A (10)(5/5)	9-15 months	12-18 months
		Sham (10)(5/5)	9-15 months	12-18 months
		BoNT-A + RAD001 (15)(5/10)	9-15 months	12-18 months
		RAD001 (15)(5/10)	9-15 months	12-18 months
		BoNT-A + RAD001 + FUOX (48)(24/24)	9-15 months	12-18 months
		RAD001 + FUOX (48)(24/24)	9-15 months	12-18 months
		BoNT-A + CPI-613 (8)(5/3)	9-15 months	12-18 months
		CPI-613 (8)(5/3)	9-15 months	12-18 months
		BoNT-A + CPI-613 + FUOX (12)(6/6)	9-15 months	12-18 months
		CPI-613 + FUOX (12)(6/6)	9-15 months	12-18 months
		BoNT-A + RAD001 + CPI-613 (25)(13/12)	9-15 months	12-18 months
		RAD001 + CPI-613 (25)(13/12)	9-15 months	12-18 months
		BoNT-A + RAD001 + CPI-613 + FUOX (31)(15/16)	9-15 months	12-18 months
		RAD001 + CPI-613 + FUOX (31)(15/16)	9-15 months	12-18 months
		Age-matched controls (32)(15/17)	9-15 months	12-18 months
		Age-matched controls (32)(15/17)	9-15 months	12-18 months
Clinical trial	GC patients	Endoscopic injection of BoNT-A (6)	49-84 years	2 years follow-up

 # group from previous study (Zhao et al., 2014)

Table S13. Metabolites involved with DNA/protein synthesis, related to Figure 4 and Data S3. Effects of vagotomy (unilateral vagotomy, UVT) on gastric tissue levels (scaled intensity) of metabolites that are involved in DNA/protein synthesis in either wild-type (WT) or gastric cancer (GC) mice

	WT	**WT (UVT)**	***p*-value**	**GC**	**GC (UVT)**	***p*-value**
	Mean ± SEM	**Mean** ± SEM		**Mean** ± SEM	**Mean** ± SEM	
Choline	**1.0382** ±0.0347	**0.9399** ±0.0421	0.0039	**1.1583** ±0.0950	**1.0341** ±0.0902	0.0179
Creatine	**0.9675** ±0.0329	**0.871** ±0.0323	0.0077	**1.1146** ±0.0439	**1.0931** ±0.0385	0.3415
Cytidine	**1.016** ±0.024	**0.769** ±0.0346	0.0001	**1.2553** ±0.0882	**1.1472** ±0.0387	0.1217
Glycine	**1.0762** ±0.0582	**0.8745** ±0.0509	0.0006	**1.3519** ±0.1394	**1.1159** ±0.0929	0.0054
Histidine	**0.9938** ±0.0471	**0.8598** ±0.0725	0.0035	**1.115** ±0.0848	**1.0622** ±0.0791	0.2282
Sarcosine	**1.0912** ±0.0896	**0.8637** ±0.0898	0.0031	**1.1428** ±0.0949	**0.9587** ±0.1357	0.0182
Serine	**1.0827** ±0.0352	**0.914** ±0.0451	0.0022	**1.0947** ±0.0744	**0.9801** ±0.0546	0.0499
Threonine	**1.0502** ±0.0332	**0.8572** ±0.0248	0.0012	**1.2261** ±0.1052	**1.0057** ±0.0528	0.0059
Uracil	**1.0101** ±0.0383	**0.8603** ±0.0359	0.0015	**1.0947** ±0.0694	**1.0704** ±0.0292	0.3945

One-way ANOVA was used for comparisons between WT and WT (UVT) or between GC and GC (UVT).

Table S14, Chemical and reagent list, related to methods. List of reagents and chemicals used.

Name	Cat. no	Supplier	Country
DMSO	D8418	Sigma-Aldrich	Oslo, Norway
Cell Counting Kit-8 (CCK-8)	96992-3000TESTS-F	Sigma-Aldrich	St. Luis, MO, USA
Cell Count Reagent SF	07553-44	Nacalai tesque	Tokyo, Japan
DMEM (no glucose, no glutamine,, no pyruvate, no phenol red)	08456-65/A14430-01-500ML	Nacalai tesque/Gibco by Life Technologies	Tokyo, Japan/Grand Island, NY
DMEM	A14430-01-500ML		
RPMI-1640 with L-Gln (0.3 g/L, 2.0 mM), phenol red	R8758-500ML	Sigma-Aldrich	Norway
D-glucose			
FBS	F7524	Sigma-Aldrich	Norway
Dialyzed FBS	26400-036	Gibco by Life Technologies	USA
L-Gln	G7513-100ML	Sigma Aldrich	Norway
Glutamine/glutamate detection kit	GLN-1	Sigma-Aldrich	Saint Louis, Missouri, USA
Glutamic Dehydrogenase (L-GLDH)	G5900	Sigma-Aldrich	Saint Louis, Missouri, USA
Glutaminase	G8880	Sigma-Aldrich	Saint Louis, Missouri, USA
NAD	N9268	Sigma-Aldrich	Saint Louis, Missouri, USA
Acetate buffer, 0.5 M, pH 5	A4433	Sigma-Aldrich	Saint Louis, Missouri, USA
Adenosine 5'-Diphosphate (ADP), 100 mM, 1 ml	A4558	Sigma-Aldrich	Saint Louis, Missouri, USA
Hydrazine Hydrate, 3ml	H0883	Sigma-Aldrich	Saint Louis, Missouri, USA
L-glutamine	G6275, 2 mM	Sigma-Aldrich	Saint Louis, Missouri, USA
L-glutamate	G6150, 1 mM	Sigma-Aldrich	Saint Louis, Missouri, USA
RNase A	R4875-100MG	Sigma Aldrich	Oslo, Norway
Propidium Iodide	P4170-10MG	Sigma Aldrich,	Oslo, Norway
Triton-X	T9284	Sigma Aldrich	Oslo, Norway
Sodium acetate buffer (10 mM, CH3COONa, MW: 82.03, pH 5.2)			
Tris-HCl buffer (1M, NH2C(CH2OH)3; MW: 121.14, pH 8.0).			

Tris-EDTA Buffer	T3161		
PBS	BR0014G	Oxoid	Hampshire, England
D-PBS	14249-24	Nacalai-Tesque	Tokyo, Japan
Trypsin-EDTA	T4049-500ML	Sigma-Aldrich	Oslo, Norway
Penicillin/Streptomycin cocktail	P4333-100ML	Sigma-Aldrich	Norway
Botox ®	100U	Botox Allergan Inc.	Norway
RAD001 (also known as Everolimus)	Trl-eve	InvivoGen	San Diego, CA, USA
CPI-613 (also known as Devimistat)	SML0404-25MG	Sigma-Aldrich	Oslo, Norway
Fluorouracil (5-FU)	50 MG/ML, vnr. 137864	Hospira	Illinois, USA
Oxaliplatin	5 MG/ML, vnr. 137098	Hospira	Illinois, USA
NucleoSpin® RNA	June 2015, Rev. 17	Macherey-Nagel	
Beta-Mercaptoethanol	M3148-100ML	Sigma-Aldrich	Oslo, Norway
Bulk beads (1.4 mm/2.8mm Zirconium oxide beads)	03961-1-103/03961-1-102	Precellys 24, Bertin Technologies	France
Illumina TruSeq Stranded mRNA Library Prep kit	20020594	Illumina	
Sodium Pyruvate 110.00 mg/L, 1.0 mM		Nacalai tesque/Sigma Aldrich	Tokyo, Japan/Oslo, Norway
Isoflurane	Baxter		
Viscotears ® eye gel		Thèa	Berlin, Germany

Table S15, Description of Metabolon QC samples, related to methods.

Type	Description	Purpose
MTRX	Large pool of human plasma maintained by Metabolon that has been characterized extensively.	Assure that all aspects of Metabolon process are operating within specifications.
CMTRX	Pool created by taking a small aliquot from every customer sample.	Assess the effect of a non-plasma matrix on the Metabolon process and distinguish biological variability from process variability.
PRCS	Aliquot of ultra-pure water	Process Blank used to assess the contribution to compound signals from the process.
SOLV	Aliquot of solvents used in extraction.	Solvent blank used to segregate contamination sources in the extraction.
DS	Derivatization Standard	Assess variability of derivatization for GC/MS samples.
IS	Internal Standard	Assess variability and performance of instrument.
RS	Recovery Standard	Assess variability and verify performance of extraction and instrumentation.

Transparent Methods

GC patients

Twenty-two patients (17 men aged 49-87 years and 5 women aged 51-83 years) were included. 16 of 22 patients underwent total/subtotal or distal gastrectomy because of intestinal or diffuse gastric cancer and were followed-up for 5 years since 2012 at St. Olavs Hospital, Trondheim, Norway. The study was approved by the Regional Committees for Medical and Health Research Ethics Central Norway (REK 2012-1029). 6 of 22 patients were enrolled in a clinical trial (see below) (Table S12). Total, subtotal or distal gastrectomy was performed on 16 patients diagnosed with gastric cancer. Biopsies from 4 pre-determined positions in corpus (major and minor curvature), cardia and antrum were collected, and largest diameter of the tumor was decided. Biopsies from adjacent, normal tissue was taken 5-10 cm from the tumor site. TNM status was defined, and samples were classified according to Lauren's classification, (Intestinal, diffuse or mixed/combined type), WHO classification (tubular, papillary, mucinous and poorly cohesive), WHO grading (well, moderately or poorly differentiated), and were reviewed according to the Japanese pathological classification. Samples were assigned gastric histopathology scoring including inflammation, epithelial defects, oxyntic atrophy, epithelial hyperplasia and dysplasia and an overall GHAI score.

Animals

Three hundred-twenty four mice were used and some of the mice were followed- up for more than one year to measure the overall survival rate. The mouse GC model was the transgenic INS-GAS mice which spontaneously develop GC at our own institute (Wang et al., 1996; Zhao et al., 2014) and its wild-type (WT) mice (FVB strain). Mice were housed ~5 mice per cage on wood chip bedding with a 12-hour light/dark cycle in a specific pathogen free environment with room temperature of 22°C and 40-60% relative humidity. Mice including both INS-GAS and WT mice were age-matched and randomized into different experimental groups (Table S12). All animal experiments were approved by The Norwegian Food Safety Authority (Mattilsynet).

Surgery

Vagotomy and BoNT-A injections were performed under isoflurane anesthesia as described previously(Zhao et al., 2014). The success of UVT was confirmed by reduced thickness of gastric mucosa (Zhao et al., 2014) and reduced tissue-levels of metabolites that are involved in DNA/protein synthesis in the denervated side in comparison with the innervated side of stomach (Table S13).

Chemicals and reagents

For details, see chemical and reagent list in Table S14.

Cells and cell culture

GC cell lines included AGS (female, 54 years, Caucasian), MKN74 (male, 37 years, Asian), MKN45 (female, 54 years, Caucasian) and KATO-III (male, 55 years, Asian). AGS cells were kindly provided by Prof. Sasakawa (Tokyo University, Japan). MKN45 cells were kindly provided by Prof. Kamiya (Kyorin University, Japan). MKN74 cells were provided by Prof. T.C Wang and KATO-III cells were purchased from LGC group.

AGS and MKN45 cells were maintained in Dulbecco's Modified Eagle's Medium (DMEM (1.0 g/l Glucose, 10 mM) with L-Gln (584.00 mg/L, 4.0 mM) and Sodium Pyruvate (110.00 mg/L, 1.0 mM)(Nacalai tesque, Japan) supplemented with 10% fetal bovine serum (FBS; ThermoFisher Scientific, Grand Island, NY) and antibiotic-antimycotic solution (1%) containing penicillin, streptomycin and amphotericin B (Nacalai tesque, Japan). MKN74 and KATO-III cells were maintained in RPMI-1640 medium (Sigma Aldrich, Norway) supplemented with fetal bovine serum (10%, FBS), Sodium pyruvate and penicillin streptomycin solution (1%) in a humidified incubator holding 5% CO_2 and 37°C.

In vitro experiments

Gln/pyr depletion

The cells ($1.0x10^4$) were plated (24h) and treated with 0-2.0 mM L-glutamine and 1.0 mM pyruvate in DMEM supplemented with dialyzed bovine serum (10%) and glucose at 25 mM. In depletion testing, either glutamine or pyruvate were omitted from the medium. Proliferation was assessed using Cell Count Reagent SF or Cell counting Kit-8 reagent at 450 nm and cell proliferation was calculated relative to controls. Determination of endogenous L-glutamine and L-glutamate was performed after 1, 6 and 24 hrs in culture using a detection kit (Glutamine/glutamate determination kit, Sigma, Saint Louis, Missouri).

Drug screen

Cells ($2.5x10^3$) were plated (24 hrs) and subjected to individual dose-response drug screens and sequential combination treatment during 3 days in culture. First, cells were treated with either serum-free medium or BoNT-A- without serum at 0.25 U BoNT-A/well and incubated for 24 hrs. CPI-613 and RAD001 were dissolved in DMSO at highest solubility before diluted in the medium. The cells were treated with RAD001, CPI-613, combination of these or vehicle (DMSO) control and incubated for 24 hrs. A combination of 5-FU and oxaliplatin or medium control was added to the cells for 24 hrs. To assess whether the drug combinations acted synergistically, we calculated Bliss synergy scores for RAD001 + CPI-613 combinations using the SynergyFinder web-application (Ianevski et al., 2017). Synergy scores were quantified as an average excess over expected drug combination effect given by the Bliss reference model (Ianevski et al., 2019). Bliss Independence model was used because the two drugs (i.e. RAD001 and CPI-613) act independently in such a manner that neither of them interferes with the other (different sites of action), but each contributes to a common result, i.e. cell proliferation.

In vivo experiments

GC mice were injected BoNT-A through laparoscopic procedure as described earlier (Zhao et al., 2014), treated with RAD001 (1.5 mg/kg/day for 3 weeks, i.p.), CPI-613 (20 mg/kg/week, once weekly for 3 weeks, i.p.), or combination of RAD001 and CPI-613. Saline injection (i.p.) was used as control. The mice were allowed one-week rest after the first cycle of treatment, and then the treatment cycle was repeated once, yielding a total treatment window of 8 weeks (**Figure 7H**). BoNT-A was dissolved in saline containing methylene blue (1.0 %) to visualize the injection. The achieved

concentration of BoNT-A was 0.25 U of BoNT-A/mL. Injection was performed through laparotomy into the serosa layer in the anterior side of stomach. Thus, for a mouse receiving 0.4 mL BoNT-A (0.25 U/mL) the dose corresponded to 0.10 U. 5-Fluorouracil (5-FU) was given i.p. at dose of 25 mg/kg in a volume of 0.5 mL. Oxaliplatin was given i.p. at dose of 5 mg/kg in volume of 0.5 mL. The two drugs were injected on either left or right side of abdomen at same time once weekly for 3 weeks in 2 cycles, starting one week after BoNT-A injection.

Sample collection and preparation

Mouse tissue samples were taken after the animals were killed under deep isoflurane inhalation anesthesia. The anterior and posterior parts of stomachs were collected for histopathological analysis and cryopreservation for transcriptomics of mouse GC in which mice underwent unilateral vagotomy (UVT) at 6 months of age and the stomachs were collected 6 months afterwards, the data from our previous study was re-analyzed (according to 3R principle)(Zhao et al., 2014). For metabolomics, GC and WT mice at 6 months of age underwent the same UVT or sham operation and the stomachs were collected as described previously. Six months after UVT, animals were terminated for sampling, and tissue samples from the denervated anterior stomach and tissue samples from the posterior stomach with intact innervation were analyzed with liquid chromatography/mass spectrometry and gas chromatography/mass spectrometry. Mouse tissue samples were collected for transcriptomics analysis immediately after completing two months BRC-treatment.

Measurement of survival rate, body weight and tumor size

Animals were followed up by daily inspection with scoring sheet, weighing and euthanized according to primary human endpoints. Scoring parameters included severe body weight loss (>25%), stress behavior, abdominal pain or reduced physical activity and was followed in collaboration with the responsible veterinarian at the animal facility. Body weight was measured daily (during treatment) or weekly (during follow up). Tumor volume density (% of glandular area of the stomach occupied by tumor) was measured using point count method described earlier[14].

Pilot clinical trial (phase II)

Six patients were enrolled according to inclusion criteria and written consent (Supplementary Data: Clinical Trial Protocol). Inclusion criteria included 1) patients who received 1st line and 2nd line chemotherapy but no longer respond to such therapy, 2) patients who, due to toxicity of chemotherapy, could not be offered such treatment, 3) patients who, after meticulous information about chemotherapy, still did not want such treatment and 4) patients with performance status (ECOG) 0-2. Patients were elderly and diagnosed with already advanced gastric cancer which precluded surgical resection (Table S12). Exclusion criteria included 1) known allergy to any of the components in Botox®, 2) known peripheral motor neuropathy disease (for example: Amyotrophic Lateral Sclerosis, ALS), or subclinical or clinical deficiency of neuromuscular transmission (for example: Myasthenia Gravis or Eaton-Lambert`s Syndrome), 3) another cancer disease that is not under control, 4) another concomitant treatment for cancer, 5) serious mental illness and 6) performance status (ECOG) 3-4. One patient with TNM status T3N0M0 was rejected for surgery due to comorbidity following a short period with neoadjuvant chemotherapy. At the time of

enrollment into this study, 4 out of 6 patients had metastatic disease, and 2 of these patients had extensive liver metastasis with short expected life expectancy. Extensive tumor masses in the stomach were present in 3 out of 6 patients. The patients were admitted to the hospital shortly after the baseline CT scan, and endoscopic BoNT-A injection was performed under sedation with midazolam. One hundred units with Botox® were diluted into 14 mL saline by the Department for Clinical Studies at St.Olav Hospital's Pharmacy. This amount was divided into 7 doses of 2 mL (14.3 U/dose) that were injected at 4 sites around the tumor and at 3 sites directly into the tumor. Some of the patients had advanced and extensive tumor masses in the stomach and for those patients, injections were concentrated to the area of the stomach with measurable tumor thickness or diameter, omitting the rest of the tumor masses in the stomach. After the endoscopic procedure, the patients were observed in the surgical ward and discharged from hospital the day after the procedure. Primary outcome measures were assessment of tumor size (volume density and/or thickness) in the stomach using standardized CT protocols after 2, 8 and 20 weeks. Two weeks after the injection, the patients had an outpatient clinical visit with complete physical assessment, specially emphasizing on detecting any adverse or toxic events related to the experimental treatment. At 8 and 20 weeks after the injection, another thoracic and abdominal CT scan was performed, together with a follow-up outpatient clinical examination. Secondary outcomes included toxicity (within 2- and 8-weeks post injection) and performance status (ECOG) after 2, 8 and 20 weeks. The safety evaluation was performed based on the CTC (Common Toxicity Criteria) criteria. The study was conducted in accordance with the guidelines for GCP (Good Clinical Practice) and it was approved by the Regional Committee for Medical and Health Research Ethics (2012/1031) and the Norwegian Medicines Agency (2012-002493-31).

Transcriptomics

Total RNA was extracted from harvested stomachs of mice or surgical biopsies of patients. RNA quality and quantity were obtained using NanoDrop One (Thermo Scientific, Norway) and Agilent Bioanalyser. RNA sequencing of human GC samples was performed using Illumina platform as described earlier[14], whereas RNA sequencing of mouse samples was performed using Illumina HiSeqNS500 instrument (NextSeq 500) at 75 bp with paired end (PE) reads using NS500H flowcells with 25 M reads/sample. Paired end forward read length (R1): 81, reverse read length (R2): 81. Illumina microarray data was analyzed using Lumi on the log2 scale and was analyzed using the empirical Bayesian method implemented in Limma. Gene expression was analyzed using a t-test between cancer and WT mice or between tumor and normal adjacent tissue in patients. Transcripts with a *p*-value of less than 0.05 were considered to be differentially expressed. Benjamini-Hochberg false discovery rates were included.

Metabolomics

Metabolomics was performed using a platform that incorporates two separate ultrahigh-performance liquid chromatography/tandem mass spectrometry (UHPLC/MS/MS2) injections and one gas chromatography/mass spectrometry (GC/MS) injection per sample by Metabolon (USA). Identification, relative quantification, data-reduction and quality-assurance components of the process were

included in the analysis platform. 343 metabolites were identified (Data S3). The informatics system consisted of four major components, the Laboratory Information Management System (LIMS), the data extraction and peak-identification software, data processing tools for QC and compound identification, and a collection of information interpretation and visualization tools for use by data analysts. The hardware and software foundations for these informatics components were the LAN backbone, and a database server running Oracle 10.2.0.1 Enterprise Edition. For more details, see description of Metabolon QC samples in Table S15.

Real-time PCR

Total RNA was isolated and purified using an Ultra-Turrax rotating-knife homogenizer and the mirVana miRNA Isolation Kit (AM1560, Ambion) according to the manufacturer's instructions. Mouse WNT pathway RT2 profiler PCR array was used (StepOnePlusTM, Applied Biosystems), which targeted key genes involved in the canonical and non-canonical WNT pathway and endogenous genes for reaction control (89 genes and 7 controls, see Table S1). The reaction was performed according to the manufacturer's instructions (SABiosciences Corporation, QIAGEN Norway).

Data visualization

R/Bioconductor environment was used to process omics-data before differential expression analysis. Graphical data visualization and data analyses were carried out using GraphPad Prism software 6.0 (GraphPad Software, U.S), Excel 2016 (Microsoft), IPA (Qiagen, Aarhus, Denmark) and RStudio version 3.5.2 (2018-12-20). Diagram plots in Figure 5 were created with JavaScript library D3.js v.4. SPSS v.23-25 was used to perform test statistics including *t*-tests and non-parametric tests, one-way ANOVA, and correlation/linear regression analyses. Heatmaps were encoded in RStudio using the heatmap.2 function. Single-cell data were processed using Seurat v3 (doi.org/10.1016/j.cell.2019.05.031) and visualized in a tSNE plot (Figure 3). IPA was used to cluster cell-specific marker genes to WNT/mTOR-glutamine-dependent gene markers in Figures 8C-D and Figures S6A-E.

Ingenuity Pathway Analysis (IPA)

Transcriptomics and metabolomics datasets were analyzed using IPA (Qiagen, Hilden, Germany) which has sophisticated algorithms and criteria to calculate predicted functional activation/inhibition of canonical pathways, diseases and functions, transcription regulators and regulators based on their downstream molecule expressions (QIAGEN Inc., https://www.qiagenbioinformatics.com/products/ingenuitypathway-analysis). For human GC microarray, Illumina identifiers (ILMN) were uploaded together with log_2-fold change, *p*-values and *q*-values (false discovery rates). A total of 47,323 transcripts was assigned to analysis. A total of 37,489 transcripts were mapped/9,834 transcripts unmapped by IPA. For RNA sequencing, Ensembl identifiers were uploaded together with log_2-fold change, *p*-values and q-values. A total of 54,460 transcripts was assigned to analysis. A total of 53,735 was mapped/725 unmapped by IPA. For mouse GC microarray, ILMN were aligned together with log_2-FC and q-values before

uploaded in IPA. A total of 12,519 transcripts was loaded, a total of 11,773 transcripts was mapped/746 unmapped in IPA. For metabolomics, HMDB and KEGG identities were aligned together with fold changes, expressed *p*-values and *q*-values. A total of 343 metabolites were uploaded for downstream analysis in IPA and 252 metabolites were mapped by IPAThe data was subjected to a metabolomics expression analysis using HMDB or KEGG as identifier type. One-way ANOVA was used between groups. Fold changes were inverted before IPA analyzes. Thus, a molecule with 0.5-fold change was negatively inverted (-1/0.5) to -2.0.

Regulatory z-scores for canonical pathways that overlapped with our experimental data were calculated using the formula described previously (Krämer et al., 2014). To generate the network of up- or down-regulated genes, custom-made molecular networks were developed based on information contained in the IPAs knowledge base. Networks of these genes were then algorithmically generated based on their interrelationships. Filtering of datasets included species, *p*-value cut-off and/or *q*-value cut-offs. Molecular networks and canonical pathways were algorithmically constructed based on known connectivity and relationships among metabolites and genes/proteins using IPAs knowledge base. The significance of the association between the dataset molecules and the canonical pathways was measured by Fischer's exact test that was used to calculate a *p*-value determining the probability that the association between the genes in the dataset and the canonical pathway by chance alone. Z-scores were calculated in IPA based on the dataset's correlation with the activated state. Negative z-scores indicate a decrease in activity, positive z-scores indicate an increase in activity. Canonical pathways were identified using statistical cut-offs at $p<0.05$ and/or $q<0.05$.

In silico experiment

Signaling pathways of WNT/β-catenin and mTOR were constructed based on the transcriptomic data of INS-GAS mice and were then entered into the "Pathway" module of the IPA to obtain the nodes in every corresponding signaling pathway. The expression data from INS-GAS *vs.* FVB mice (Mouse GC *vs.* WT) was compared to all genes in the pathways. Nodes were added as entries into the "My list"-function and all entries in the list were added to the "My pathway" in IPA. My pathway was used to produce a network of nodes/genes from the WNT and mTOR signaling pathways that matched with our experimental data from INS-GAS *vs.* FVB. The build-tool was used to connect nodes using edges, i.e. relationships including both direct and indirect interactions like chemical-protein interactions, ubiquitination, molecular cleavage, translocation, localization, phosphorylation, expression, protein-protein interactions, activation, regulation of binding, inhibition, membership, reaction, protein-DNA interactions, transcription and modification. The Canonical Pathway overlay-tool was used to arrange the entries into two clusters based on pathway. Next, the molecule activity predictor (MAP)-function was used to predict activation/inhibition between the nodes in the network. The *in silico* tool was employed to predict effects on the network after gene inhibition. Categorical values were set to each gene/node using a semi-quantitative method to quantify the color-change resulting from *in silico* inhibition. Dark blue colored nodes were represented by -2, light blue as -1, white as 0, light orange

as +1 and dark orange as +2. Values are represented of n=7-14 experiments per inhibition node/gene.

Upstream regulator analysis

Ingenuity pathway analysis (IPA, QIAGEN) was used to perform upstream analysis of the transcriptomics datasets based on the literature and the Ingenuity Knowledge Base. The analysis examines how many known targets of the upstream regulators are present in the dataset. An overlap *p*-value is computed based on significant overlap between genes in the dataset and known targets regulated by the transcriptional regulator. The activation z-score algorithm is used to make predictions. In mouse GC, 144 regulators were found to be activated (z-score>2, $p<0.05$) based on the expression levels of target molecules in the datasets. The overlay-tool in the "My pathway" module was used to cluster the activated regulators into canonical pathways. Next, upstream regulators of interest were added into custom-made pathways in the Path Designer-tool and relationship-types between upstream regulator and target molecule were added.

tSNE plot of metabolic gene expression according to single-cell atlas

Available data on a single-cell transcriptome network of gastric premalignant and early gastric cancer in patients was utilized (PMID: 31067475), including 13 biopsies from 9 patients: 3 mild superficial gastritis (NAG), 3 chronic atrophic gastritis (CAG), 6 intestinal metaplasia (IM), and 1 early gastric cancer (EGC). Single-cell data were processed using Seurat v3 (doi.org/10.1016/j.cell.2019.05.031) and normalized for each of the 13 samples independently. The functions FindIntegrationAnchors, IntegrateData, ScaleData and RunPCA with default parameters were used. Cells with number of expressed genes lower than 400 or larger than 7000 and 20% or more of UMIs mapped to mitochondrial or ribosomal genes were removed. 50 PCs were utilized to visualize single-cell atlas with a tSNE plot. The expression levels of marker genes in mouse GC *vs.* WT for each representative cell type were analyzed. Marker genes were identified by differential expression analysis with the threshold as fold change > 1.5 and FDR < 0.01.

Statistics

Values are expressed as means ± SEM or SD and statistical methods are shown in the figure legends.

Supplemental references

Ianevski, A., Giri, A. K., Gautam, P., Kononov, A., Potdar, S., Saarela, J., Wennerberg, K. & Aittokallio, T. (2019). Prediction of drug combination effects with a minimal set of experiments. Nature Machine Intelligence *1*, 568-577.

Ianevski, A., He, L., Aittokallio, T. & Tang, J. (2017). SynergyFinder: a web application for analyzing drug combination dose–response matrix data. Bioinformatics *33*, 2413-2415.

Krämer, A., Green, J., Pollard, J., Jr. & Tugendreich, S. (2014). Causal analysis approaches in Ingenuity Pathway Analysis. Bioinformatics (Oxford, England) *30*, 523-530.

Wang, T. C., Koh, T. J., Varro, A., Cahill, R. J., Dangler, C. A., Fox, J. G. & Dockray, G. J. (1996). Processing and proliferative effects of human progastrin in transgenic mice. J Clin Invest *98*, 1918-29.

Zhang, P., Yang, M., Zhang, Y., Xiao, S., Lai, X., Tan, A., Du, S. & Li, S. (2019). Dissecting the Single-Cell Transcriptome Network Underlying Gastric Premalignant Lesions and Early Gastric Cancer. Cell Rep *27*, 1934-1947 e5.

Zhao, C. M., Hayakawa, Y., Kodama, Y., Muthupalani, S., Westphalen, C. B., Andersen, G. T., Flatberg, A., Johannessen, H., Friedman, R. A., Renz, B. W., et al. (2014). Denervation suppresses gastric tumorigenesis. Sci Transl Med *6*, 250ra115.